In presenting this dissertation in partial fulfillment of the requirements for an advanced degree at Idaho State University, I agree that the Library shall make it freely available for inspection. I further state that permission for extensive copying of my dissertation for scholarly purposes may be granted by the Dean of the Graduate School, Dean of my academic division, or by the University Librarian. It is understood that any copying or publication of this dissertation for financial gain shall not be allowed without my written permission.

Signature _____

Date _____

POSITRON PRODUCTION EFFICIENCY STUDY USING

HIGH REPETITION RATE LINAC AT IAC

by

Sadiq Setiniyaz

(Shadike Saitiniyazi)

A dissertation

submitted in partial fulfillment

of the requirements for the degree of

Doctor of Philosophy in the Department of Physics

Idaho State University

Jul 2013

To the Graduate Faculty:

The members of the committee appointed to examine the dissertation of Sadiq Setiniyaz (Shadike Saitiniyazi) find it satisfactory and recommend that it be accepted.

Tony Forest, Ph.D.

Major Advisor

Yujong Kim, Ph.D.

Committee Member

Dustin McNulty, Ph.D.

Committee Member

Mahbub A. Khandaker, Ph.D.

Committee Member

Wenxiang Zhu, Ph.D.

Committee Member

Acknowledgments

Thanks to my advisor Dr. Forest, who made this whole work possible. He always help me to the very details of my work patiently.

Thanks to Dr. Kim. He helped and directed me a lot on accelerator physics area of my research and experiments.

Thanks to Dr. Chouffani and Dr. Freyberger for their advise and direction in the experiments.

Thanks to engineers at IAC, especially Chad, Kevin, Brian.

Thanks to my friends Oleksiy, Jason, Mayir, Carlos, Zaijing, Olga, and Misha always there when I needed them, like lifting heavy stuff, lead bricks.

Also Thanks to my friends Chris, Jack, Tony, and many others.

Contents

List of Figures

List of Tables

Abstract

Positrons were produced using a tungsten target when impinged by an electron beam from the High Repetition Rate Linac (HRRL) at the Beam Lab of the Physics Department at Idaho State University (ISU). To measure the intensity of positrons at five (1-5 MeV) different energies, two dipoles were used to bend positrons to the second tungsten target where they annihilate and create 511 keV photons. 511 keV photons were measured using two NaI detectors placed horizontally and operated in coincidence. The positron beam creation and loss are explained with simulation studies using G4beamline. The simulation results are compared with the experiment. Although positron distribution in both simulation and experiment peaked at 3 MeV, the simulation predicted higher counts than the experiment.

Chapter 1

Introduction

1.1 Positron Beam

Positrons are used in several disciplines of sciences, like chemistry, physics, material science, surface science, biology and nanoscience [1]. Different approaches are used to generate positrons. The main challenge is increasing the intensity (or current) of the positron beam. One of the most common methods used to generate a positron beam is using an electron linac. The electron beam produces a positron beam by bremsstrahlung and pair production. One of the advantages of the linac based positron beam is its variable energy and intensity.

1.1.1 Positron Beam for Positron Annihilation Spectroscopy

Positron annihilation spectroscopy is a non-damaging technique to detect defects in materials. It is based on the fact that positrons tend to annihilate near defects in the material [2]. Different depths of the materials can be probed by using variable energy positron source and a linac based variable energy positron source may be used for this purpose.

1.1.2 Positron Beam for Measuring The Impact of Two Photon Exchange

The nucleon electromagnetic form factors are fundamental quantities that are related to the charge and magnetization distribution in the nucleon. Conventionally, the nucleon form factors are measured using the Rosenbluth Technique (RT) [3]. The form factor scaling ratio, $R = \mu_p G_{Ep}/G_{Mp}$, is measured using this technique is around unity as shown (hollow square)

in Figure 1.1 [4]. Since the 1990's, a technique using elastic electron-proton polarization transfer to measure this ratio has been developed [4–6]. In this technique, form factor scaling ratio linearly decreases as the Q^2 increases, as shown (circle) in Figure 1.1.
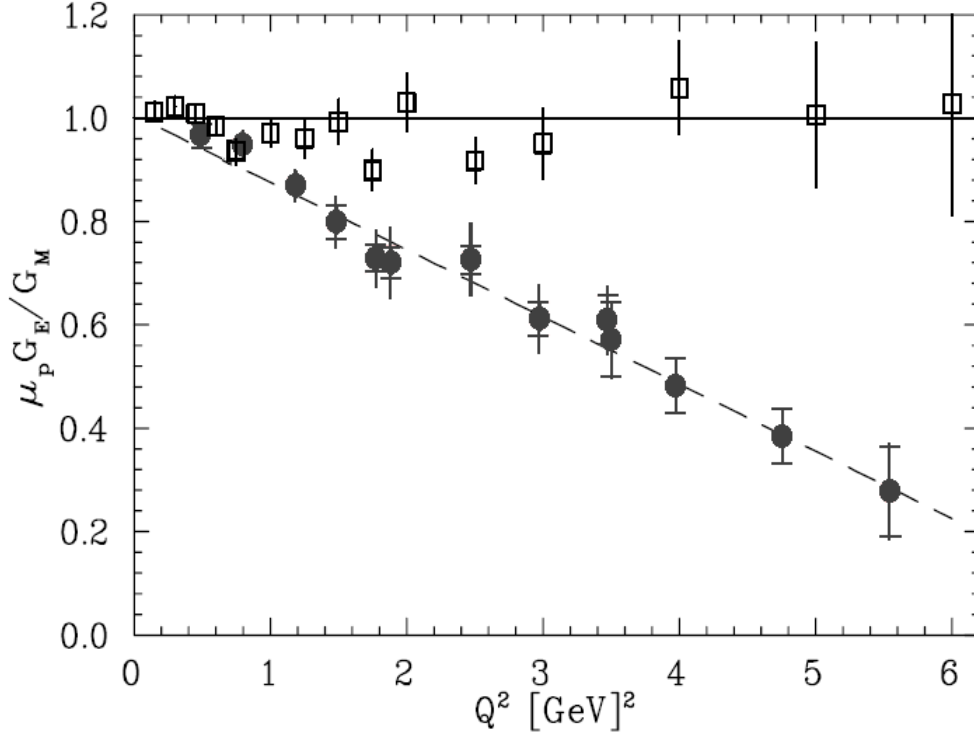
Figure 1.1: Form factor ratio, obtained by Rosenbluth Technique (hollow square) and results from Recoil Polarization Technique [5].

The disagreement could arise from the fact that the Rosenbluth Techqniue assumes that only One Photon Exchange (OPE) occurs during the scattering while the Two Photon Exchange (TPE), which depends weakly on Q^2, could also become considerable with increasing Q^2 [5]. The contribution of TPE can be obtained by comparing the ratio of e^+ p to e^- p scattering. The interference of OPE and TPE can also be studied in the scattering process $e^+e^- \rightarrow p\bar{p}$.

1.2 Positron Beam Generation from Bremsstrahlung

When a moving charged particle interacts with the electric field of another charged particle, it can be deflected and lose energy in the form of photons, as shown in Figure 1.2. This interaction is known as the bremsstrahlung process. The probability of this interaction increases with the atomic number of the material traversed by the incident charged particle. Figure 1.3 shows the photon energy distribution produced when the 12 MeV electron energy distribution from Figure 1.4 interacts with a 1 mm thick tungsten target. As shown in Figure 1.3, the distribution peaks at 0.3 MeV. As the photon energy increases the number of photons produced decreases.
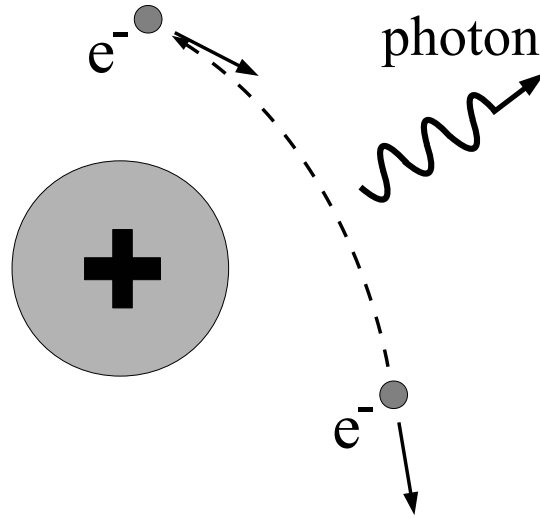
Figure 1.2: Photon generation from bremsstrahlung processes.

The bremsstrahlung cross section given is by [7]

$$d\sigma = 4Z^2 r_e^2 \alpha \frac{d\nu}{\nu} \left\{ \left(1 + \left(\frac{E}{E_0} \right)^2 \right) \left[\frac{\phi_1(\gamma)}{4} - \frac{1}{3} \ln Z - f(Z) \right] - \frac{2E}{3E_0} \left[\frac{\phi_2(\gamma)}{4} - \frac{1}{3} \ln Z - f(Z) \right] \right\},$$

$$(1.1)$$

where E_0 is initial total energy of the electron, E is final total energy of the electron, $\nu = \frac{E_0 - E}{h}$ is frequency of the emitted photon, and Z is atomic number of the target. $\gamma = \frac{100 m_e c^2 h\nu}{E_0 E Z^{1/3}}$ is charge screening parameter and $f(Z)$ is given by

$$f(Z) = (Z\alpha)^2 \sum_{1}^{\infty} \frac{1}{n[n^2 + (Z\alpha)^2]}, \tag{1.2}$$

where $\alpha = \frac{1}{137}$ is fine-structure constant, ϕ_1 and ϕ_2 are screening functions that depend on Z.
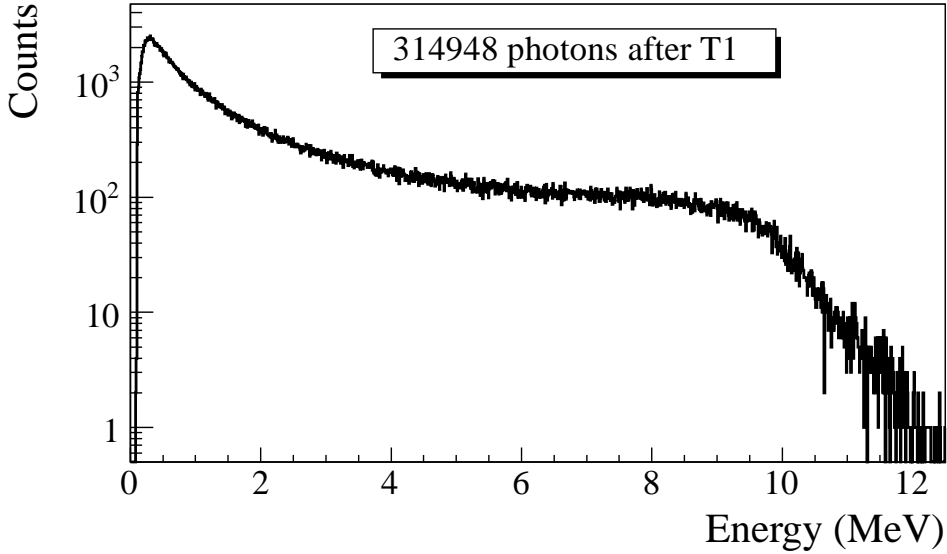
Figure 1.3: Bremsstrahlung photon energy right after a tungsten foil in simulation.

There are three competing processes that a photon can undergo when interacting with matter. Figure 1.5 is the cross-sections for different types of photon interactions with tungsten as a function of photon energy. At electron volt (eV) energies which is comparable to the electron atomic binding energy, the dominant photon interaction is via the photoelectric effect. As the photon energy increases up to kilo electron volt (keV) range, the Compton scattering process starts to be more dominant. Although the photon is totally absorbed during the photoelectric effect, photons merely lose energy when undergoing the Compton

4
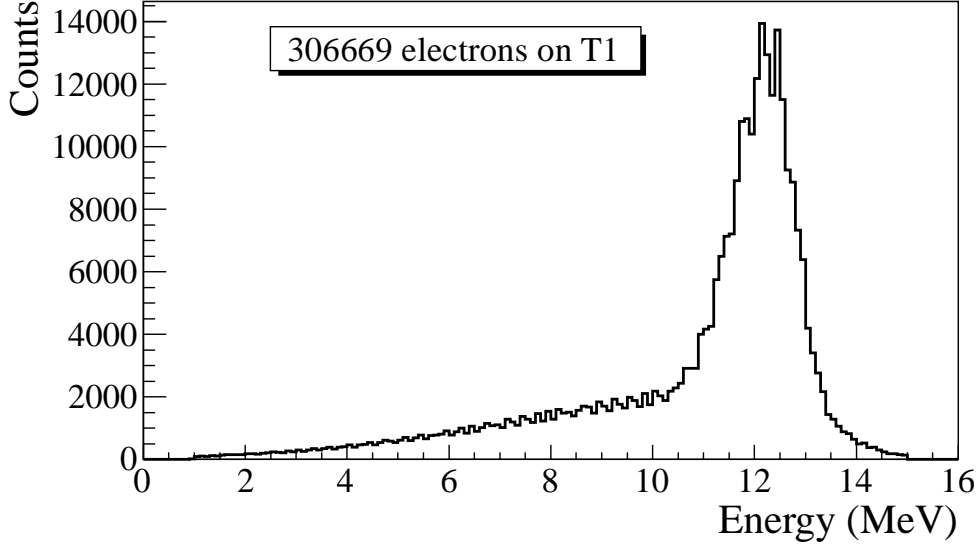
Figure 1.4: The electron energy distribution incident on a tungsten foil in simulation.

scattering. As the photon energy reaches twice the rest mass energy of the electron, *i.e.* $2 \times$ 511 keV, the pair production begins to occur. The pair production becomes the dominant interaction process when photon energies are beyond 5 MeV [8]. In this process, a photon interacts with the electric field of the nucleus or the bound electrons and is converted into an electron and positron pair.

Using natural unit, where $c \equiv 1$, the differential cross-section for pair production can be expressed as

$$\frac{d\sigma}{d\epsilon_1 d\theta_1 d\theta_2} = 8 \left(\frac{\pi a}{\sinh(\pi a)} \right)^2 \frac{a^2}{2\pi} \frac{e^2}{\hbar c} \left(\frac{\hbar}{m_e c} \right)^2 \frac{\epsilon_1 \epsilon_2}{k^3} \theta_1 \theta_2$$

$$\times \left\{ \frac{V^2(x)}{q^4} \left[k^2 (u^2 + v^2) \xi \eta - 2\epsilon_1 \epsilon_2 (u^2 \xi^2 + v^2 \eta^2) + 2(\epsilon_1^2 + \epsilon_2^2) u v \xi \eta \cos(\phi) \right] \right. \tag{1.3}$$

$$\left. + a^2 W^2(x) \xi^2 \eta^2 \left[k^2 (1 - (u^2 + v^2) \xi \eta - 2\epsilon_1 \epsilon_2 (u^2 \xi^2 + v^2 \eta^2) - 2(\epsilon_1^2 + \epsilon_2^2) u v \xi \eta \cos(\phi) \right] \right\} ,$$

where k is photon energy, θ_1 and θ_2 are the scattering angle of e^+ and e^- respectively, $\phi = \phi_1 - \phi_2$ is the angle between the e^+ and e^- pair, ϵ_1 and ϵ_2 are the energy of the positron
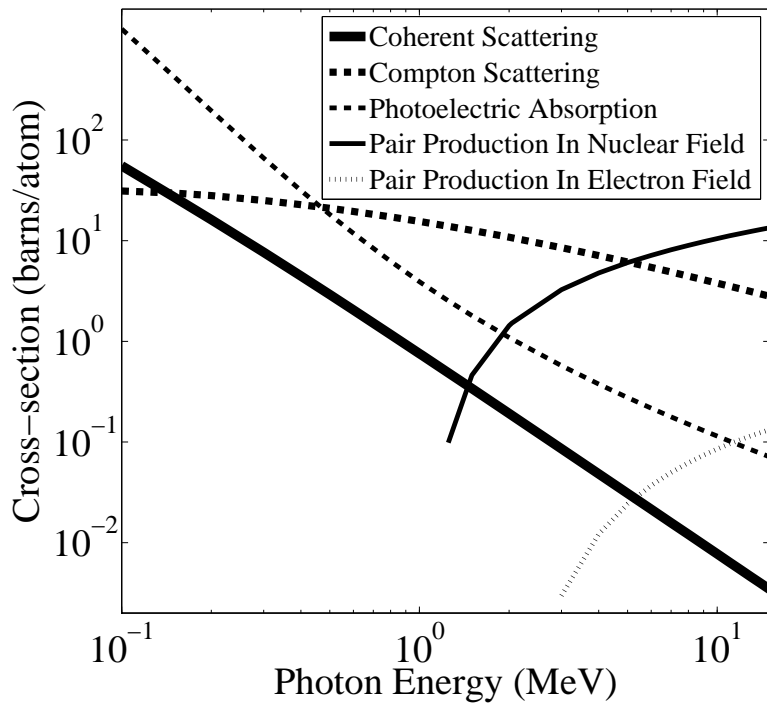
Figure 1.5: The cross-sections for different types of photon interactions with tungsten as a function of photon energy [9].

and electron respectively. Other constants are $u = \epsilon_1 \theta_1$, $v = \epsilon_2 \theta_2$, $\xi = \frac{1}{1+u^2}$, $\eta = \frac{1}{1+v^2}$, $q^2 = u^2 + v^2 + 2uv \cos(\phi)$, $x = 1 - q^2 \xi \eta$, $a = \frac{Ze^2}{\hbar c}$, $V(x) = 1 + \frac{a^2}{(1!)^2} + \frac{a^2(1+a^2)x^2}{(2!)^2} + \frac{a^2(1+a^2)(2^2+a^2)x^4 x^2}{(3!)^2} + \cdots$, and $W(x) = \frac{1}{a^2} \frac{dV(x)}{dx}$.

In pair production, positron and electron pairs are created back to back in the center of mass frame. In the lab frame, electrons and positrons tend to move in the direction of the photon, as shown in Figure 1.6. The positron and electron carry away the energy from the photon that is in excess of 1.022 MeV. In the center of mass frame, the kinetic energy is equally shared. Photons with an energy above 1.022 MeV in the bremsstrahlung spectrum of Figure1.3 have the potential to create electron and positron pairs. Figure 1.7 is the simulation of 10 million 12 MeV mono energy electrons impinging on a tungsten target with 1.016 mm thickness. Turning on the annihilation process resulted in a 511 keV peak on top of the bremsstrahlung spectrum. This 511 keV peak represents photons produced when the created positrons from the pair production annihilate with atomic electrons inside the tungsten target.
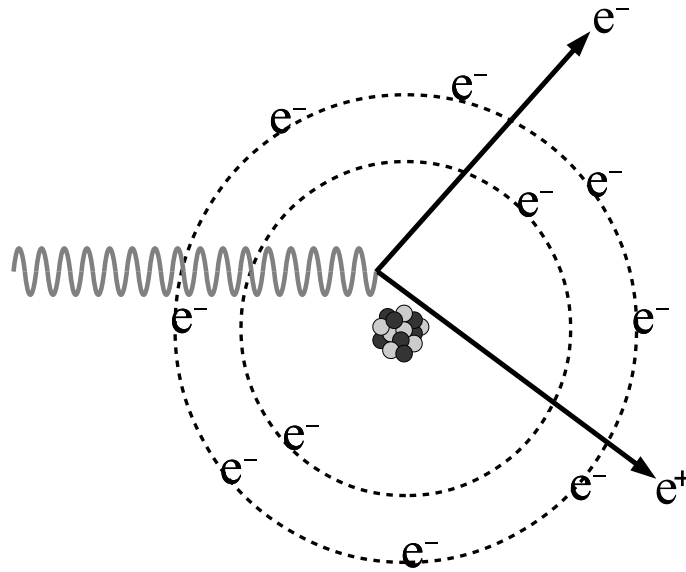
Figure 1.6: Pair production.
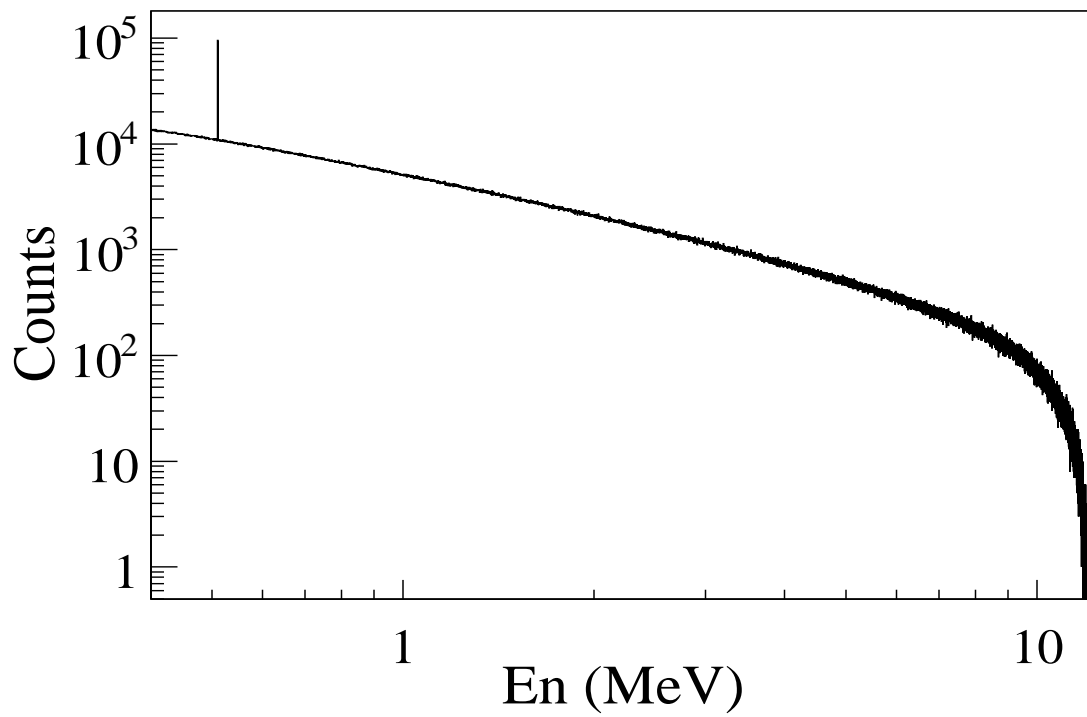
Figure 1.7: Photon spectrum of created by million 12 MeV mono energy electrons impinging on a 1.016 mm thick tungsten target.

1.3   Emittance Measurement

Emittance is an important parameter in accelerator physics. When the emittance and Twiss parameters are given at the exit of the gun, one will be able to calculate the beam size and the divergence at any given point along the beamline. To study the process of positron creation, one need to know the beam size and divergence on the target. Emittance and Twiss parameters are input parameters for any accelerator simulation tools that can be used to study the experimental processes and to make predictions.

1.3.1   Emittance

In accelerator physics, Cartesian coordinate system is used to describe the motion of the accelerated particles. The z-axis of Cartesian coordinate system is defined as the natural coordinate that is going along the electron beam line. The x-axis and y-axis are horizontal and vertical coordinates which constitute the transverse beam profile. For the convenience of representation, one may use z to represent transverse coordinates and express longitudinal profile with natural coordinates s along the beamline. The transverse beam profiles are described as a function of the longitudinal coordinate, *i.e.* $x(s)$ and $y(s)$. The angle of an accelerated charge regarding the designed orbit can be defined as

$$z' = \frac{dz}{ds}. \tag{1.4}$$

The phase space z' vs. z of the beam is an ellipse with invariant area (along the beamline). This invariant is called the Courant-Snyder invariant [10]. The transverse emittance ϵ of the beam is defined to be the area of the ellipse that contains 90% of the particles. Beam divergence and Twiss parameters are related to the beam size and divergence by

$$\sigma_x(s) = \sqrt{\epsilon_x(s)\beta_x(s)}, \ \sigma_{x'}(s) = \sqrt{\epsilon_x(s)\gamma_x(s)}, \tag{1.5}$$

where ϵ_x is beam horizontal emittance, σ_x is rms beam size, $\sigma_{x'}$ is rms beam divergence, and

β_x and γ_x are two of the Twiss parameters.

1.3.2   Emittance Measurement

The HRRL beam emittance was measured using an Optical Transition Radiation (OTR). Transition radiation was theoretically predicted by Ginzburg and Frank [11] in 1946 to occur when a charged particle passes the boundary of two medium and emits radiation. An OTR based viewer was installed to observe electron beam size at the high electron currents, available using the HRRL at 15 MeV with 200 ns macro pulse width and 37.2 mA peak current. The visible light is produced when a relativistic electron beam crosses the boundary of two mediums with different dielectric constants. Visible radiation is emitted at an angle of 90° with respect to the incident beam direction when the electron beam intersects the target at a 45° angle. These backward-emitted photons are observed using a digital camera and can be used to measure the shape and the intensity of the electron beam based on the OTR distribution. Although an emittance measurement can be performed in a several ways [12, 13], the quadrupole scanning method [14] was used to measure the emittance, Twiss parameters, and beam energy in this work.

1.3.3   Quadrupole Scanning Method

Fig. 1.8 illustrates the beamline components used to measure the emittance for the quadrupole scanning method. A quadrupole is positioned at the exit of the linac to focus or de-focus the beam as observed on the OTR view screen. The 3.1 m distance between the quadrupole and the screen was chosen in order to minimize chromatic effects and to satisfy the thin lens approximation. Assuming the thin lens approximation, $\sqrt{k_1}L << 1$, is satisfied, the transfer matrix of a quadrupole magnet may be expressed as

$$\mathbf{Q} = \begin{pmatrix} 1 & 0 \\ -k_1 L & 1 \end{pmatrix} = \begin{pmatrix} 1 & 0 \\ -\frac{1}{f} & 1 \end{pmatrix}, \tag{1.6}$$

10
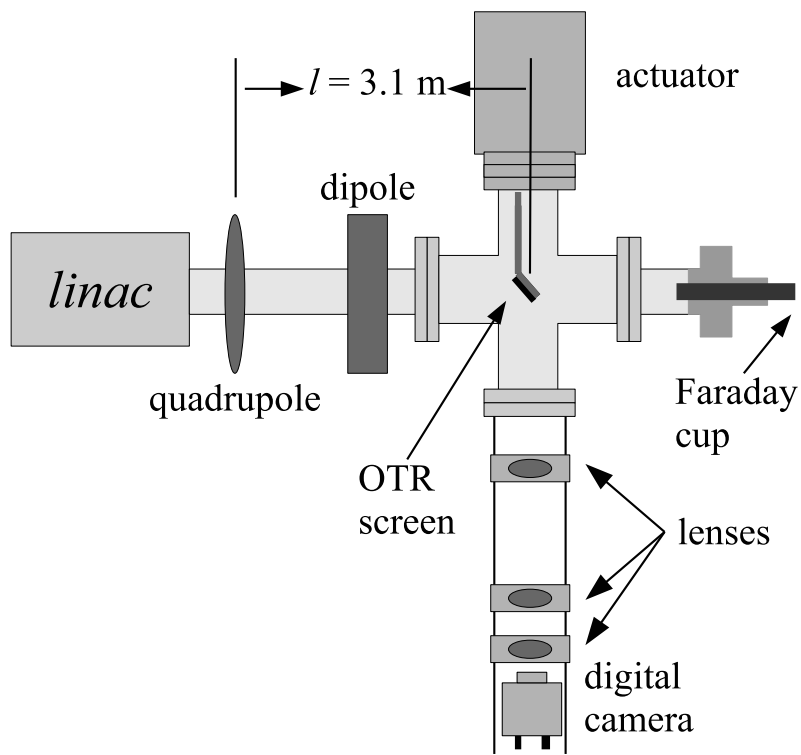
Figure 1.8: Apparatus used to measure the beam emittance.

where k_1 is the quadrupole strength, L is the length of quadrupole, and f is the focal length. A matrix representing the drift space between the quadrupole and screen is given by

$$\mathbf{S} = \begin{pmatrix} 1 & l \\ 0 & 1 \end{pmatrix}, \tag{1.7}$$

where l is the distance between the scanning quadrupole and the screen. The transfer matrix $\mathbf{M}$ of the scanning region is given by the matrix product $\mathbf{SQ}$. In the horizontal plane, the beam matrix at the screen $(\sigma_\mathbf{s})$ is related to the beam matrix of the quadrupole $(\sigma_\mathbf{q})$ using the similarity transformation

$$\sigma_\mathbf{s} = \mathbf{M}\sigma_\mathbf{q}\mathbf{M}^\mathrm{T}. \tag{1.8}$$

where the $\sigma_\mathbf{s}$ and $\sigma_\mathbf{q}$ are defined as [15]

$$\sigma_{\mathbf{s},x} = \begin{pmatrix} \sigma_{\mathrm{s},x}^2 & \sigma_{\mathrm{s},xx'} \\ \sigma_{\mathrm{s},xx'} & \sigma_{\mathrm{s},x'}^2 \end{pmatrix}, \ \sigma_{\mathbf{q},x} = \begin{pmatrix} \sigma_{\mathrm{q},x}^2 & \sigma_{\mathrm{q},xx'} \\ \sigma_{\mathrm{q},xx'} & \sigma_{\mathrm{q},x'}^2 \end{pmatrix}. \tag{1.9}$$

By defining the new parameters [14]

$$A \equiv l^2 \sigma_{\mathrm{q},x}^2, \ B \equiv \frac{1}{l} + \frac{\sigma_{\mathrm{q},xx'}}{\sigma_{\mathrm{q},x}^2}, \ \text{and} \ C \equiv l^2 \frac{\epsilon_x^2}{\sigma_{\mathrm{q},x}^2}. \tag{1.10}$$

The matrix element $\sigma_{\mathrm{s},x}^2$, the square of the rms beam size at the screen, may be expressed as a parabolic function of the product of k_1 and L

$$\sigma_{\mathrm{s},x}^2 = A(k_1 L)^2 - 2AB(k_1 L) + (C + AB^2). \tag{1.11}$$

The emittance measurement was performed by changing the quadrupole current, which changes $k_1 L$, and measuring the corresponding beam image on the view screen. The measured two-dimensional beam image was projected along the image's abscissa and ordinate

12

axes. A Gaussian fitting function is used on each projection to determine the rms value, σ_s in Eq. (1.11). Measurements of σ_s for several quadrupole currents $(k_1 L)$ is then fit using the parabolic function in Eq. (1.11) to determine the constants A, B, and C. The emittance (ϵ) and the Twiss parameters $(\alpha$ and $\beta)$ can be found using Eq. (1.12).

$$\epsilon = \frac{\sqrt{AC}}{l^2}, \; \beta = \sqrt{\frac{A}{C}}, \; \alpha = \sqrt{\frac{A}{C}}(B + \frac{1}{l}). \tag{1.12}$$

Chapter 2

Apparatus

2.1   HRRL Beamline

A 16 MeV S-band High Repetition Rate Linac (HRRL) located at the Beam Lab of the Department of Physics, Idaho State University is used to generate incident 12 MeV electron beam on a tungsten foil. The energy of the HRRL is tunable between 3 to 16 MeV and its repetition rate variable from 1 to 300 Hz. Basic parameters of the HRRL are given in Table 2.1. As shown in Figure 2.1, the HRRL has a thermionic gun, vertical and horizontal steering magnet sets on two ends and two solenoid magnets.

The accelerator's cavity was relocated to the position shown in Figure 2.2 to provide enough space for a beam line that can transport either positrons or electrons. The beam elements are described in Table 2.2. Quadrupole and dipole magnets were added to the new beam line as well as diagnostic tools like OTR and YAG screens, Faraday cups and toroids were installed to measure the electron beam size and the current. Energy slits were installed to control energy/momentum spread of the beam after the first dipole. A retractable tungsten foil target (T1) was placed between the 1st and 2nd triplets and used to produce

Table 2.1: The Basic Parameters of the HRRL.

Parameter	Unit	Value
maximum energy	MeV	16
peak current	mA	100
repetition rate	Hz	300
absolute energy spread	MeV	2-4
macro pulse length	ns	>50
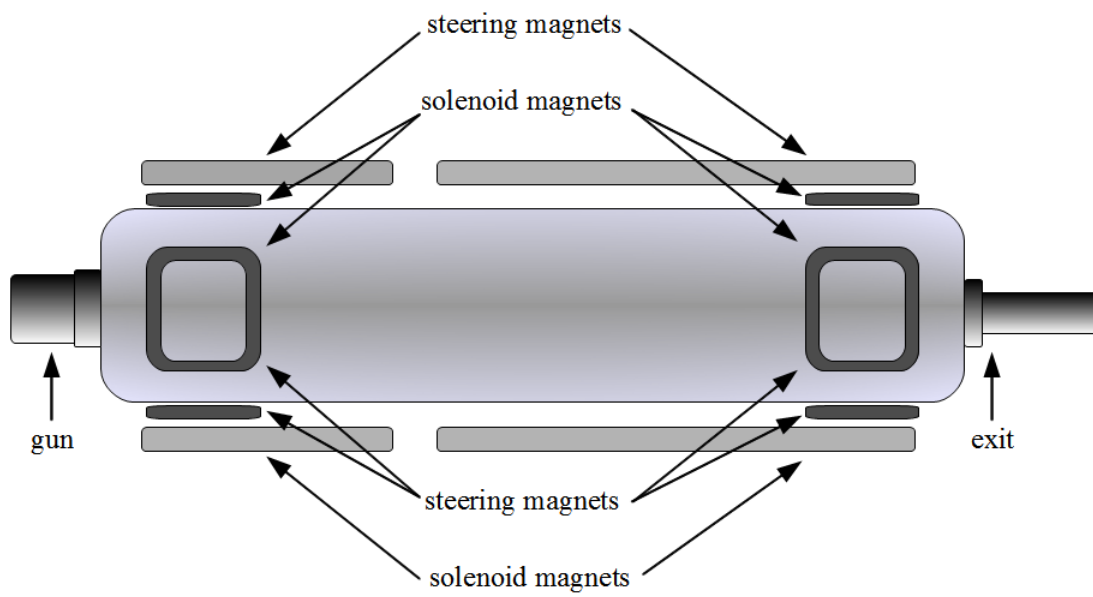
Figure 2.1: The configuration of the HRRL cavity.

Table 2.2: The HRRL Beamline Parts and Coordinates.

Label	Beamline Element	Distance from Linac Exit (mm)
Q1	quadrupole	335
Q2	quadrupole	575
Q3	quadrupole	813
T1	e^+ production target	1204
Q4	quadrupole	1763
Q5	quadrupole	2013
Q6	quadrupole	2250
D1	dipole	2680
S1	OTR screen	3570
FC1	Faraday cup	3740
EnS	energy slit	3050
S2	YAG screen	3410
Q7	quadrupole	3275
D2	dipole	3842
FC2	Faraday cup	4142
Q8	quadrupole	4044
Q9	quadrupole	4281
Q10	quadrupole	4571
T2	annihilation target	7381

positrons when the electron beam interacts with it. The room where the HRRL is located is divided by a wall into two parts; the accelerator side and the experimental cell. A beam pipe at the end of the 90 degree beamline goes through a hole on the wall and delivers the beam from the accelerator side to the experimental cell. The positron detection system consisting of two NaI detectors was placed at the end of the beamline in the experimental cell side as shown in Figure 2.2.

2.2 The OTR Imaging System

The OTR target is 10 μm thick aluminum foil with a 1.25 inch diameter. The OTR is emitted in a cone shape with the maximum intensity at an angle of $1/\gamma$ with respect to the
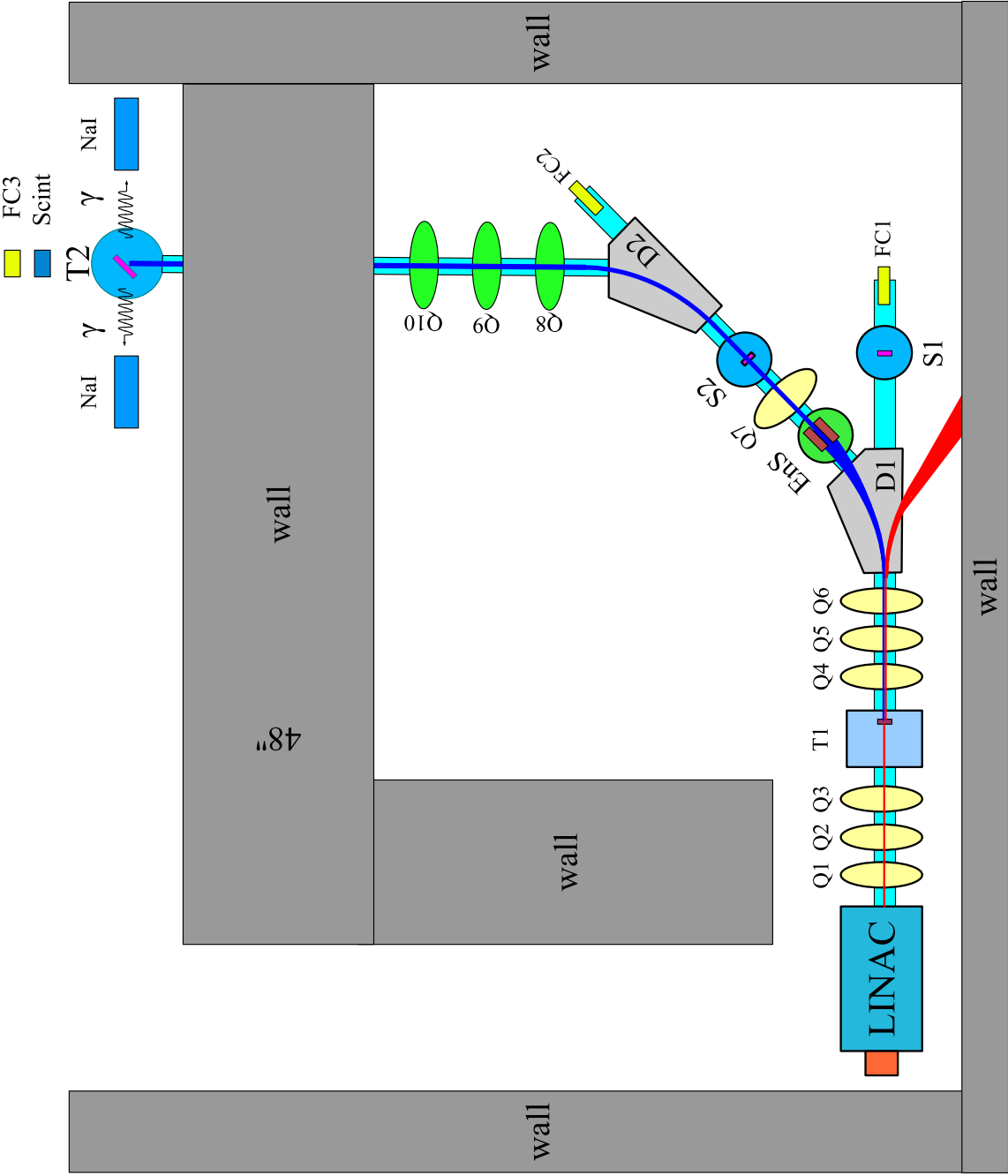
Figure 2.2: The HRRL beamline layout and parts.

reflecting angle of the electron beam [16]. Three lenses with 2 inches of diameter are used for the imaging system to avoid optical distortion at lower electron energies. The focal lengths and position of the lenses are shown in Figure 2.3. The camera used is a JAI CV-A10GE digital camera with a 767 by 576 pixel area. The images were taken by triggering the camera synchronously with the electron gun.
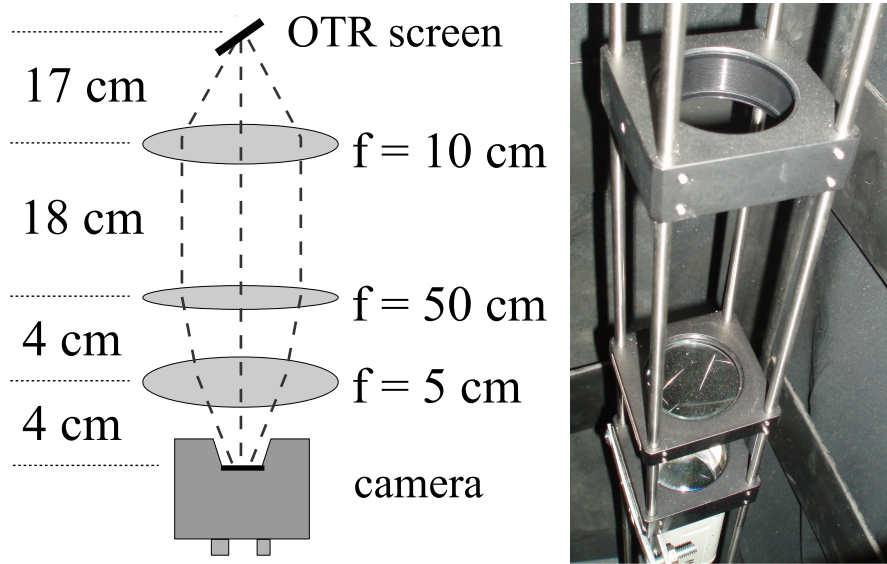
Figure 2.3: The OTR imaging system.

2.3 Positron Detection

When the electron beam is incident on T1, photon and secondary electrons are created along with positrons. These particles are the main source of noises in the experiment. The positrons were transported to the second tungsten target (T2) which was shielded from noise by the concrete wall and Pb bricks. The setup is shown in Figure 2.4. A 6-way cross was placed at the end of the beamline to hold T2. The 6-way cross has three 1 mil (0.0254 millimeters) thick stainless steel windows. The two horizontal windows perpendicular to the beamline were for the exiting of the 511 keV photons created during the positron annihilation. The one at the end of the 90 degree beamline was used as the beam exit. Two NaI detectors

were placed facing two exit windows to detect the photons produced in T2. A lead brick collimator with 2 inch diameter hole placed between the exit window and NaI detector. A scintillator and a Faraday cup were placed at the end of the beamline and were used to tune the electron and positron beam. When positrons reach T2, they are thermalized and annihilated inside T2. During the thermalization, a positron loses its kinetic energy. When it annihilates with an electron, two 511 keV photons are emitted back to back. Two NaI detectors and accelerator RF pulse are in coincidence mode to detect these back to back scattered 511 keV photons and to eliminate noises.
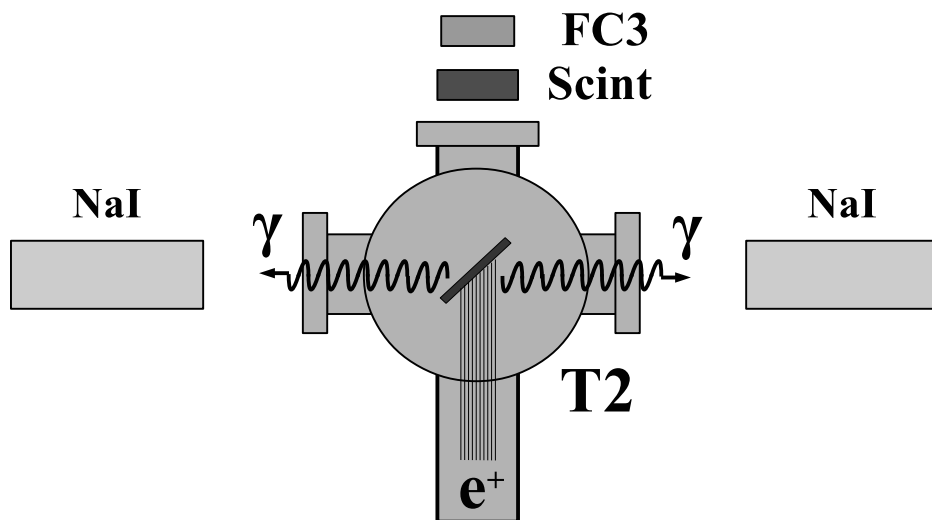
Figure 2.4: The positron detection system: T2 (pink) was placed with 45° angle to the horizontal plane first, then rotated 45° along the vertical axis.

2.3.1 NaI Detectors

NaI crystals, shown as in Figure 2.5, were used to detect 511 keV photons from positron annihilation. Originally, the detectors had pulse lengths around 400 μs. Resistors and capacitors were added to the PMT bases and pulse length is shorten to less than 1 μs. The NaI detector has one dynode and one anode outputs. The PMT base configuration of the NaI detector is shown in Figure 2.6 and bases made shown in Figure 2.7. The crystal is

Table 2.3: The Radioactive Sources and Corresponding Photon Peaks.

Radioactive Sources	Unit	First Peak	Second Peak
Co-60	keV	1173	1332
Na-22	keV	511	1275

SAINT-GOBAIN CRYSTAL & DETECTORS (MOD. 3M3/3) NaI crystal with a dimension of 3" × 3". The PMT base takes HV around -1150 V. It takes ADC 5.7 μs to convert the analog signal to a digital signal. The signal from anode was delayed 6 μs by a long cable and sent to the ADC.
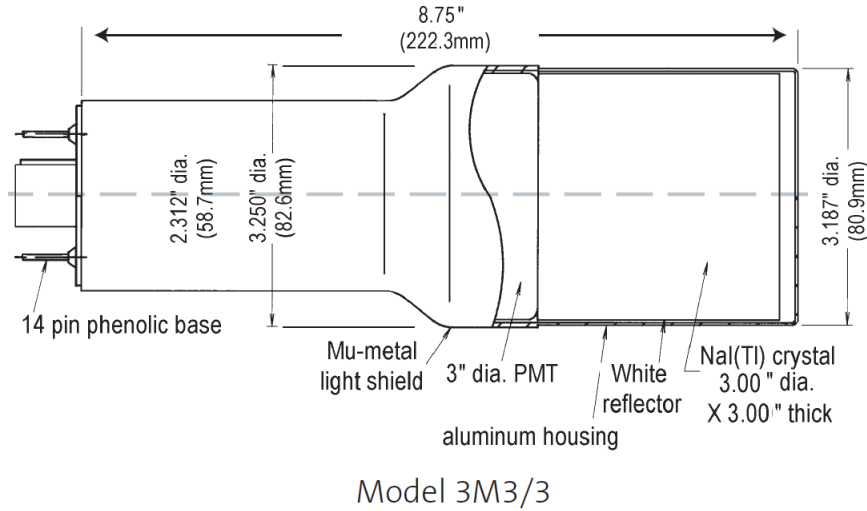
Figure 2.5: The NaI crystal dimension.

The NaI detectors were calibrated using a Na-22 and a Co-60 sources with photon peaks indicated in Table 2.3. Figure 2.8 is the oscilloscope image of Co-60 photon pulses incident on the detector with new PMT. The calibrated NaI detector spectrum of Na-22 and Co-60 sources are shown in Figure 2.9. The rms values of the fits on the four peaks shown in Figure 2.9 are $\sigma_{Na,511} = 18.28 \pm 0.04$ keV, $\sigma_{Na,1275} = 44.51 \pm 0.27$ keV, $\sigma_{Co,1173} = 42.49 \pm 0.24$ keV, and $\sigma_{Co,1332} = 50.30 \pm 0.39$ keV.

The Na-22 source was placed between two NaI detectors to photon spectrum for both when RF was on (no electrons were fired from accelerator gun) and off. The 511 keV peak
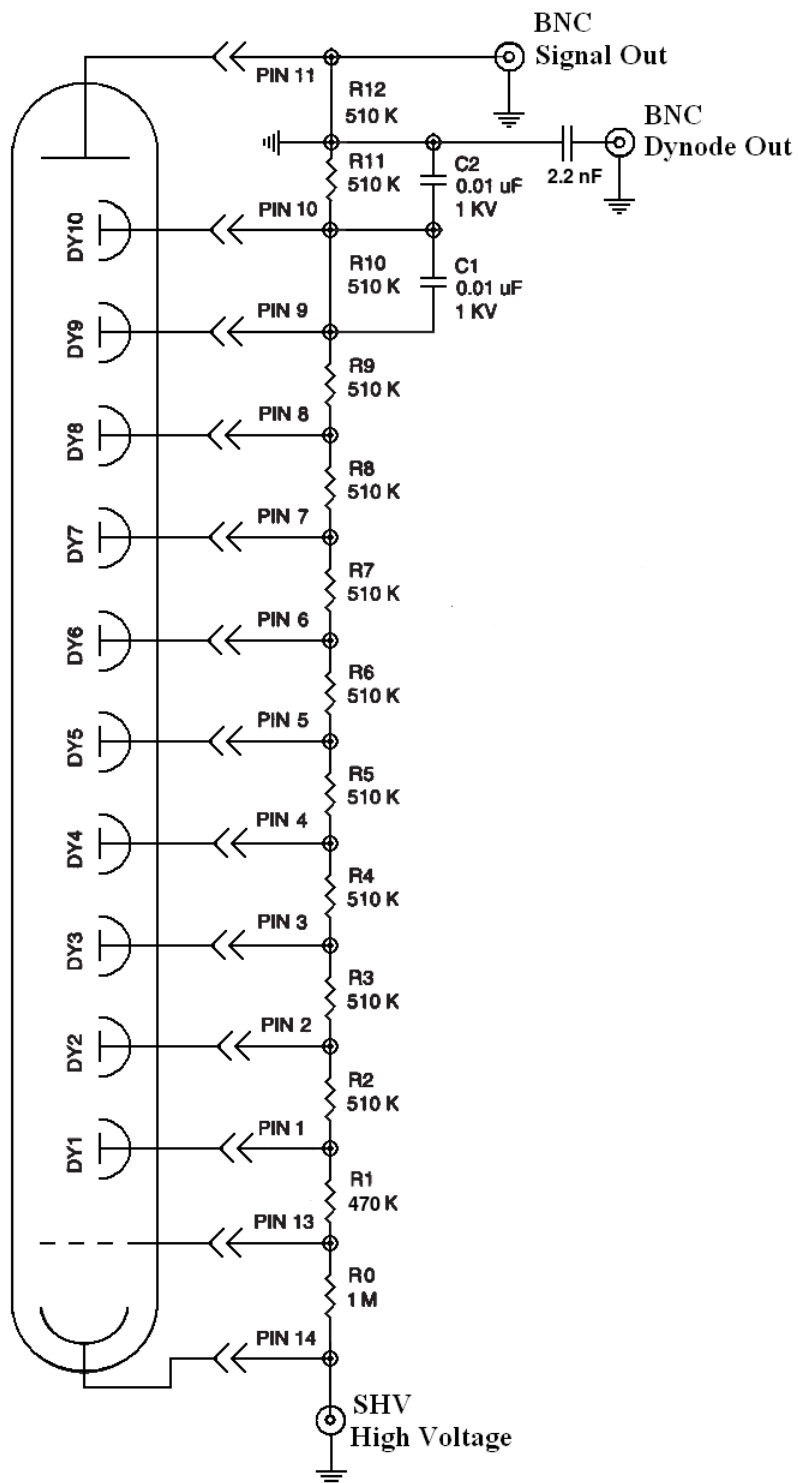
Figure 2.6: The modified PMT base design.

Figure 2.7: The NaI crystals and new bases.
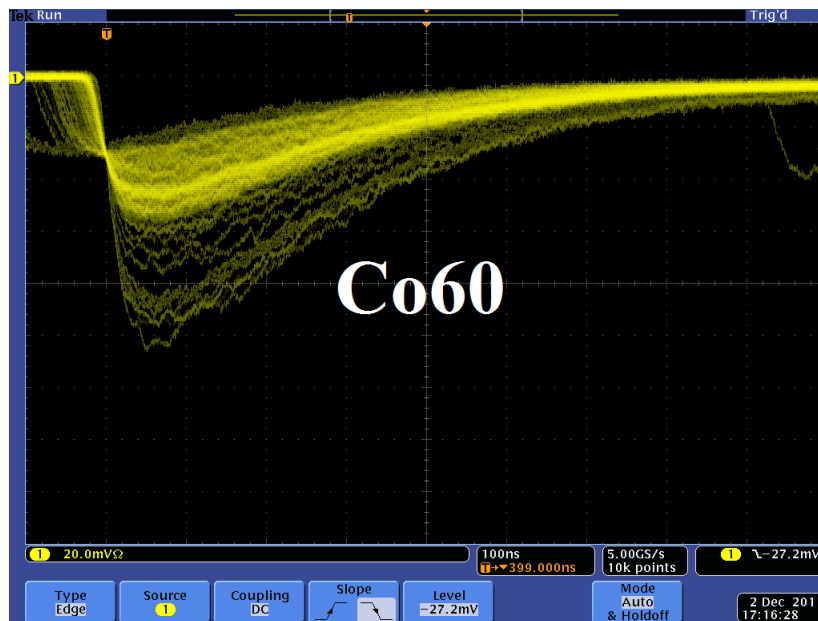
Figure 2.8: Pulses of the Co-60 source obtained using new PMT. The amplitude of of the pulse is about 60 mV. The rise time of the pulse is larger than 50 ns, and the fall time is larger than 700 ns.

Na22	
Entries	303912
Mean	621.8
RMS	303.1
Integral	2.638e+005
Constant	7731 ± 29.5
Mean	510.7 ± 0.1
Sigma	17.38 ± 0.06

Co60	
Entries	311377
Mean	879.9
RMS	361.2
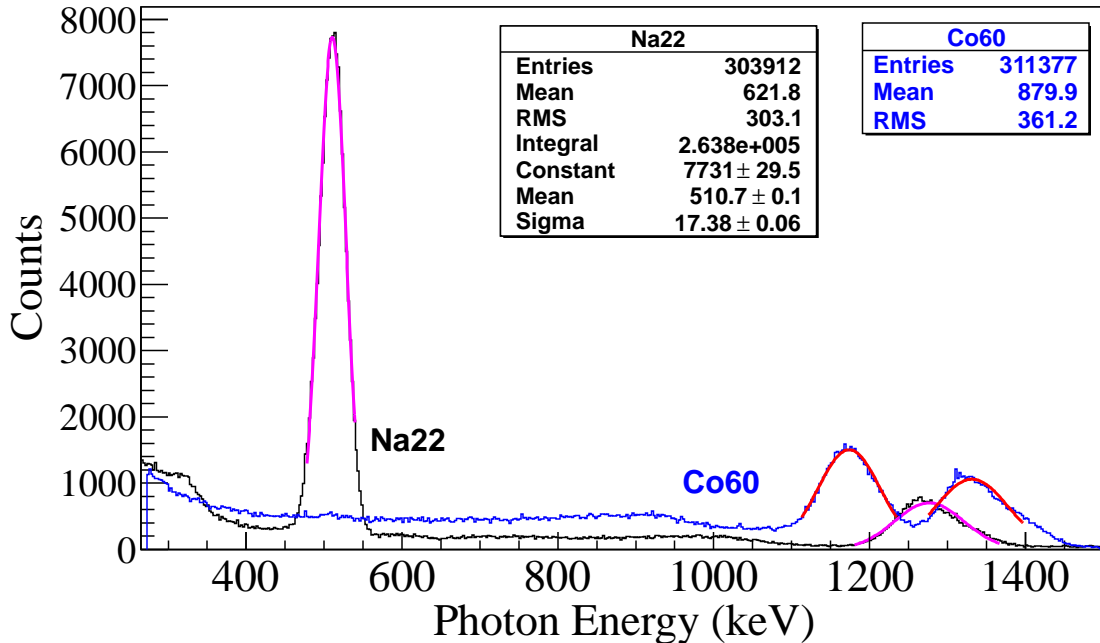
Figure 2.9: The calibrated NaI spectrum of Na-22 and Co-60 sources.

in the right NaI detector was shifted to the right side of spectrum by 17 channels when RF was on as shown in Figure 2.10 (a) while in the left NaI the peak shifted to the left by 28 channels. When 3 MeV positrons were transported to T2, the observed 511 keV peak was at the right side comparing to the peak observed in Na-22 source run with RF on. The reason of creating the shift is unclear and needs further investigation. One must keep in mind that the NaI detectors' calibration factor do change in the experiment.

2.3.2   Trigger for The DAQ

The trigger for the DAQ requires a coincidence between two NaI detectors and the electron accelerator gun pulse. The last dynode signals from left and right NaI detectors were inverted using a ORTEC 474 amplifier and sent to a CAEN Mod. N842 Constant Fraction Discriminator (CFD). The RF noise from the accelerator was as large as the signal from the NaI detector. Since it was correlated in time with the gun pulse, the gun pulse was used to generate a VETO pulse that prevent the CFD from triggering on this RF noise. After
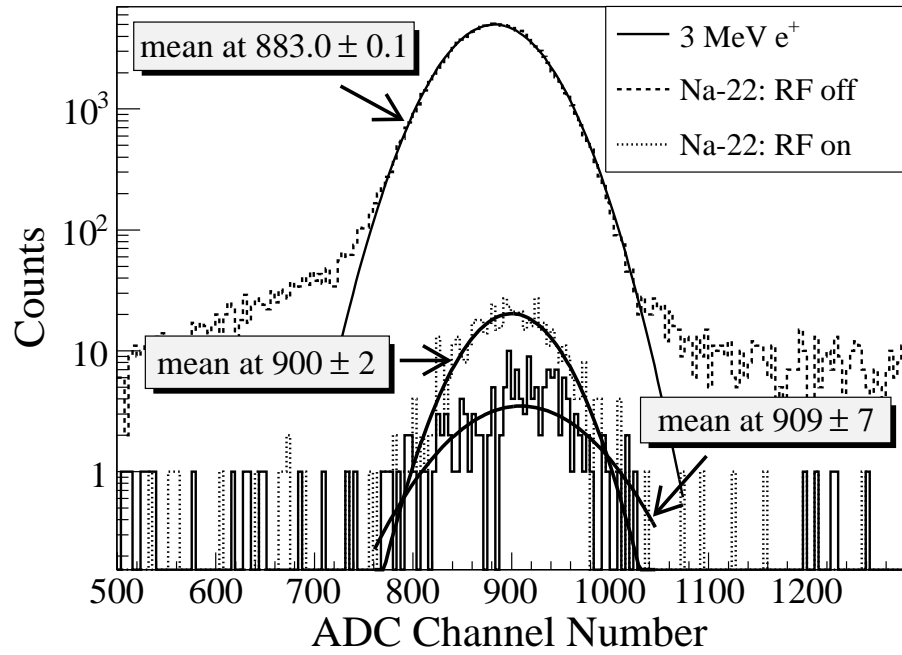
(a) Right NaI detector.
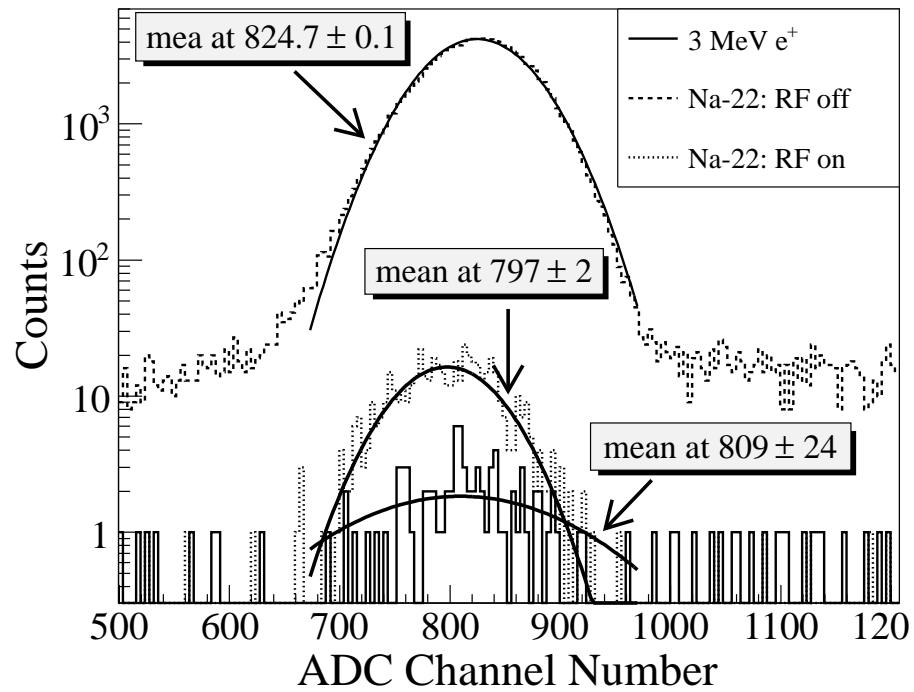
(b) Left NaI detector.

Figure 2.10: The 511 keV peak in NaI detectors shifted when RF is on.

24

this discrimination and RF noise rejection, the discriminated dynode signals were sent to an GG 8000-01 octalgate generator that increased the width of the logic signals and created one larger pulse from multiple smaller pulses. This can prevent multiple pulsing. Then the signals were sent to a LeCroy model 622 quad coincidence to generate coincident signals with the electron gun. These coincident signals sent to the third channel of the GG800-01 octalgete generator to generate coincidence between the two signals from detector and gun trigger as given by

$$(\text{NaI Left \&\& Gun Trigger}) \ \&\& \ (\text{NaI Rgiht \&\& Gun Trigger}). \tag{2.1}$$

This is to make sure that there is a trigger only when there are trigger signals from both detectors and the electron gun is firing.

The ADC was set to convert the analog signals from the NaI detectors to digital signals when the electron gun is firing. But the converted date were fast cleared unless there is a veto. The first output of the GG800-01 octalgete generator was sent to the CAEN Mod. N93B dual timer to create the veto that prevent the ADC from fast clearing the converted data. The second output of the GG800-01 octalgete generator was sent to ORTEC Gate & Delay Generator to be delayed by 6 μs, a necessary time to convert the analog signal from the anode to digital signal, and was used as the trigger for the DAQ to read data in the ADC.

Chapter 3

Simulation

Simulations were performed using G4beamline [17] to study the processes of position generation and transportation. "G4beamline is a particle tracking and simulation program based on the Geant4 [18] toolkit that is specifically designed to easily simulate beamlines and other systems using single-particle tracking [17]." The simulation predicts that at least one positron is created per 1000 incident 10 MeV electrons. A large amount of beam loss was observed during the initial simulation. As a result,the simulation was divided into three steps based on the locations along the beamline that saw more than 90% beam loss. A new beam event generator was created based on the results of the previous step in the simulation.

The first step generated an electron beam with the energy distribution that was observed in the experiment. The electrons were focused by three quadrupoles onto the target T1. Electrons transversing T1 produced bremsstrahlung photons of sufficient energy to produce e^+e^- pairs. The second step simulated the transportation of positrons exiting T1 to the entrance of the first dipole D1. The third step transported positrons from the entrance of D1 to the annihilation target T2, the interactions of positrons with T2, and the detection of the resulting 511 keV photon pairs.

3.1   Step 1 - The Electron Beam Generation and Transportation to T1

In the first simulation step, an electron beam was generated with an energy distribution that was observed in the experiment. The emittance, the Twiss parameters, and the energy

distribution of the electron beam were measured experimentally and used to generate the electron beam. The energy distribution of the electron beam is shown in Figure 4.4. The distribution was fit using two skewed Gaussian distributions. The fit parameters given in Table 4.2 were used to generated electrons.

A series of virtual detectors were placed along the beamline to sample the beam. As an example, three virtual circular detectors labeled and T1 are shown in Figure 3.1. The electron beam was detected by a virtual detector DUPT1 (Detector UPstream of T1) placed 25.52 mm upstream of T1. Positrons, electrons, and photons generated during the interaction of the electron beam with T1 were observed by virtual detectors DT1 (Detector of T1) and DDNT1 (Detector DowNstream of T1) placed 25.52 mm downstream of T1.
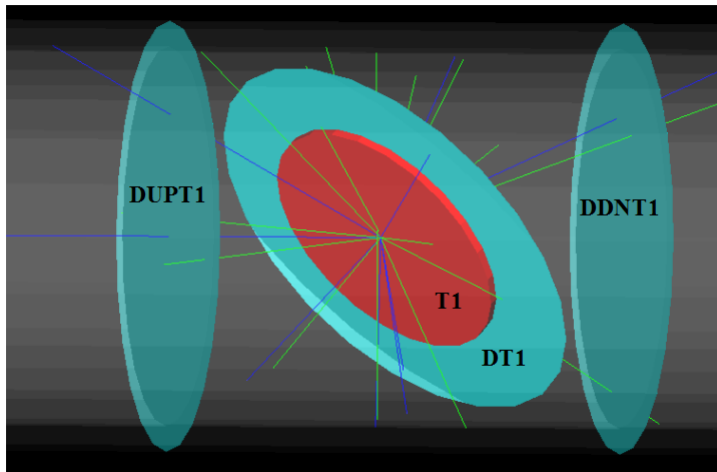
Figure 3.1: T1 is the positron production target. DUPT1 is a virtual detector located upstream of T1 to detect the incoming electron beam. DDNT1 is a virtual detector downstream of T1. DT1 is a virtual detector that is placed right after T1 parallel to it.

3.1.1   The Positron Beam on DDNT1

In the first step, 1.38×10^{10} (13799743900) electrons were generated with the energy distribution as shown by the dotted dashed line in Figure 3.2, transported to T1 and created

positrons represented by solid the line. The dashed line is the electron energy distribution observed by DDNT1. The program, ROOTSYS, crashes to draw 1.38×10^{10} electrons. The Figure 3.2 is the simulation result of 1.38×10^7 electrons incident on T1 to illustrate the energy distribution pattern. The incident electrons were detected by the virtual detector DUPT1 and downstream positrons and electrons were detected by the DDNT1.
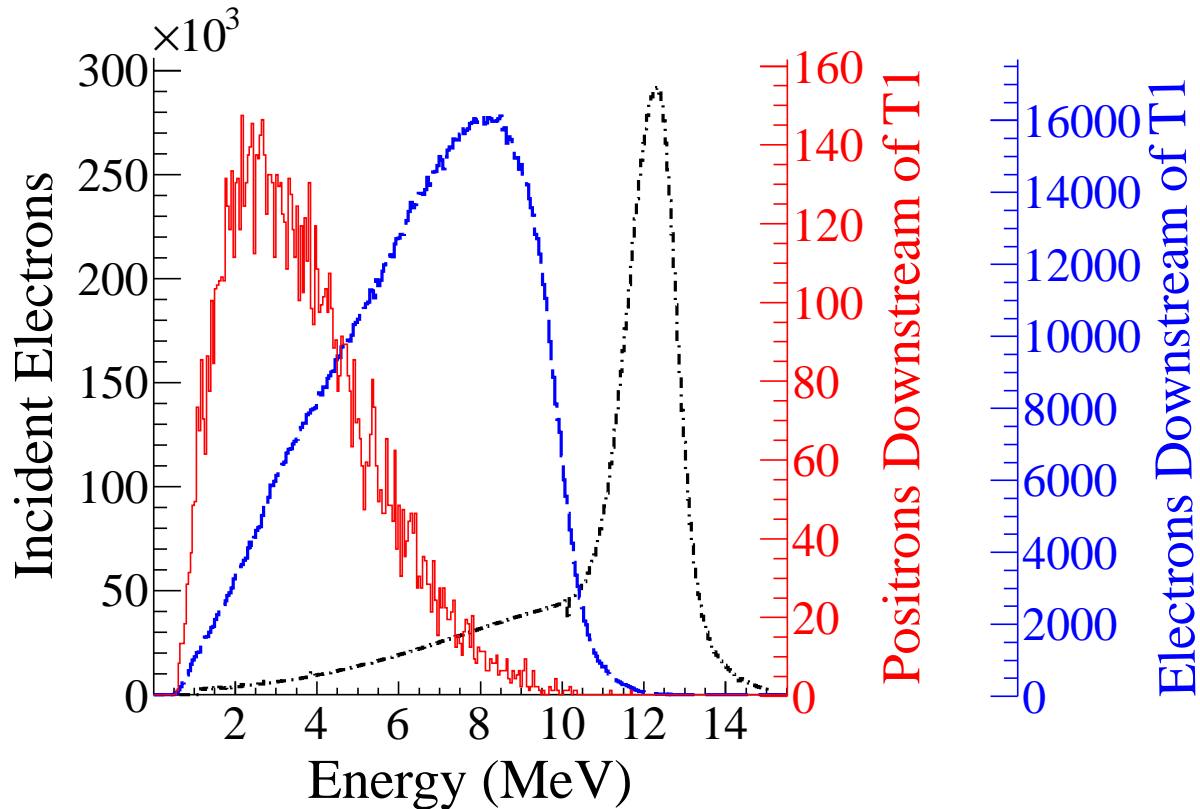
Figure 3.2: Energy distribution of incident electrons (dotted dashed line), electrons after T1 (dashed line) and created positrons (solid line).

The positron spatial distribution detected by DDNT1 is shown in Figure 3.3. The y $vs.$ x spatial distribution of the beam is shown in Figure 3.3 (e) and Figure 3.3 (f). As can be seen from Figure 3.3 (b) and (d), the y spatial distribution and divergence, defined in equation 1.4, of the positron beam have a sharp drop in counts in the region between -25.8 mm and -27.2 mm from the beam center. Figure 3.4 shows the geometry and location
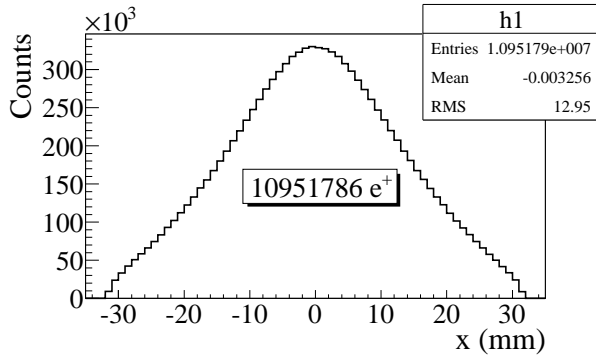
(a) x projection.
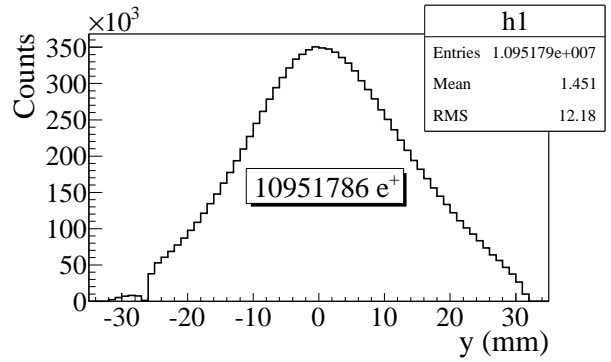
(b) y projection.
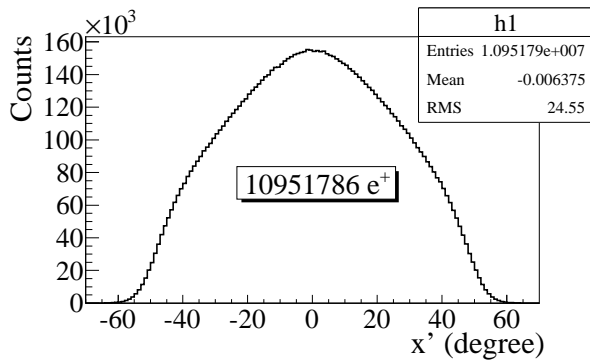
(c) x projection of the divergence.
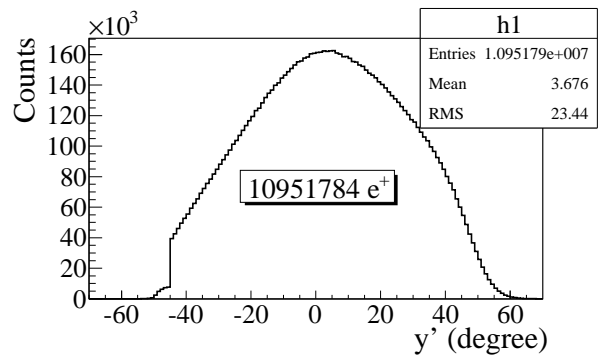
(d) y projection of the divergence.
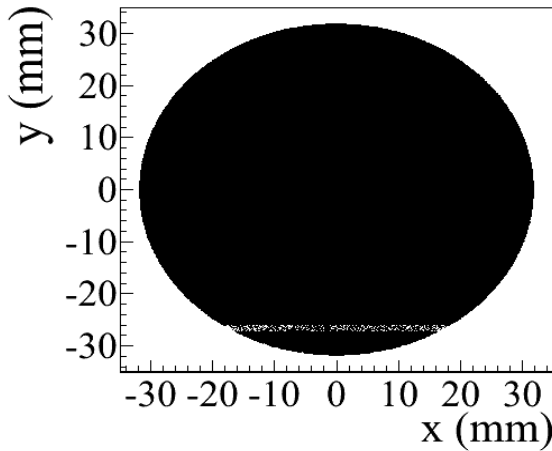
(e) The transverse beam profile.
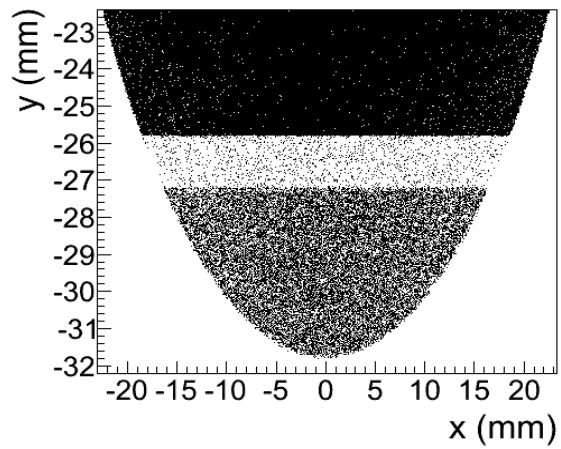
(f) The transverse beam profile zoomed in.

Figure 3.3: The transverse beam projections and angular distributions of positrons detected.

of T1 and DDNT1. If the size of T1 were to be increased, it would eventually intersect with DDNT1 at a distance between 25.8 mm and 27.2 mm from the beam center, *i.e.* the edge of the T1 is facing this 1.4 mm wide low count area.
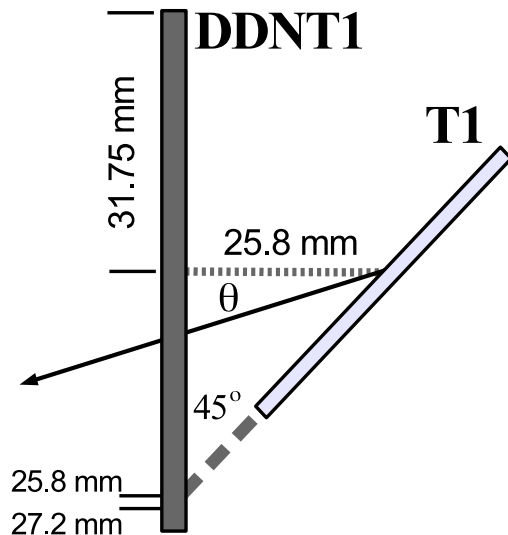
Figure 3.4: The geometry of the target T1 and the virtual detector DDNT1.

As shown in Figure 3.5, the y distribution count decreases at $\theta = 45°$. Positrons were emitted from both the downstream and upstream side of T1. Positrons from the downstream side of T1 intersected the detector at angles below $45°$ while positrons from the upstream side of T1 begin to hit the detector at angles beyond $45°$. Neither positrons upstream nor downstream of T1 traveled to the 1.4 mm wide low count area. Only positrons created on the edge of T1 reached the low count area between 25.8 mm $< x <$ 27.2 mm. Thereby, the counts in this area are lower comparatively.

3.1.2   The Positron Beam on Virtual Detectors DQ4 and DD1

The positron beam energy distribution on virtual detectors DQ4 (Detector placed at the entrance of Q4) and DD1UP (Detector placed at the UPstream entrance of D1) are shown

(a) y' *vs*. y.

(b) y' *vs*. y zoom.
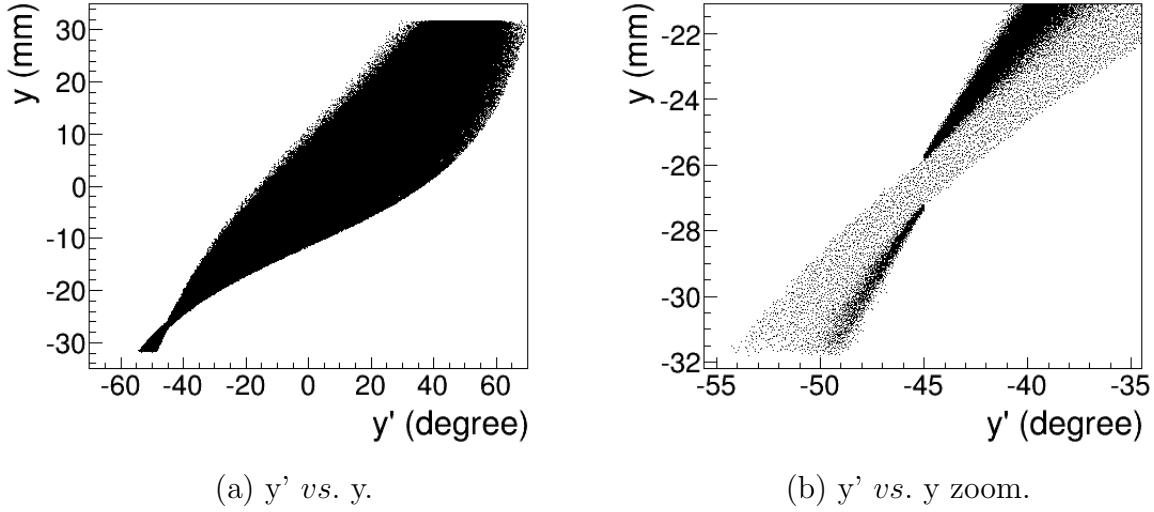
Figure 3.5: The positron beam y' *vs*. y detected by DDNT1.

in Figure 3.6. Nearly 90% of the positrons are lost when transported from DQ4 to DD1UP due to the large positrons divergence.

3.2 Step 2 - The Transportation of The Positron Beam from DDNT1 to The Entrance of The First Dipole

The beam observed on detector DDNT1 in step 1 was used to generate positrons for second step. At detector DDNT1, the higher energy positrons tend to have smaller polar angles and be closer to the beam center. Positrons were generated in 1 keV/c momentum bins with different weights, spatial, and angular distributions. The positrons are generated at DDNT1 (where they were sampled) and transported to the entrance of D1 trough a quadrupole triplet as shown in Figure 3.7. The virtual detectors were placed at the entrance of Q4 (DQ4) and D1 (DD1UP) to track the positrons. The beam observed at DD1UP would be used to generate positrons in the third step.
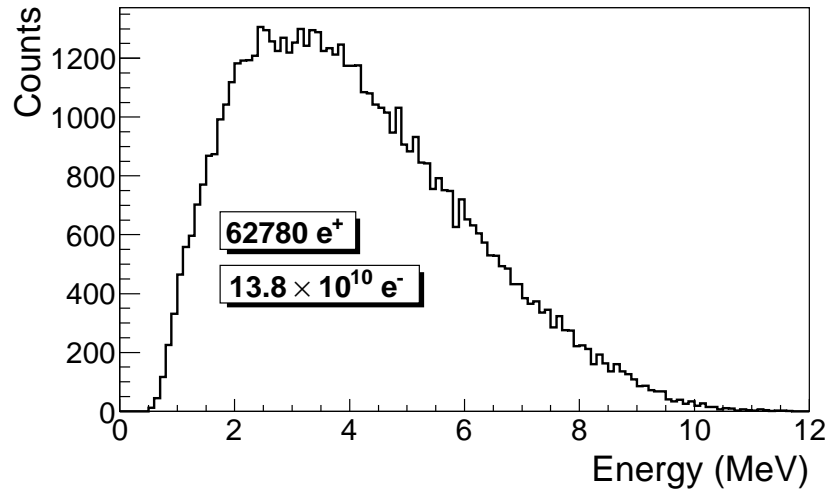
(a) The positron energy distribution on DQ4.
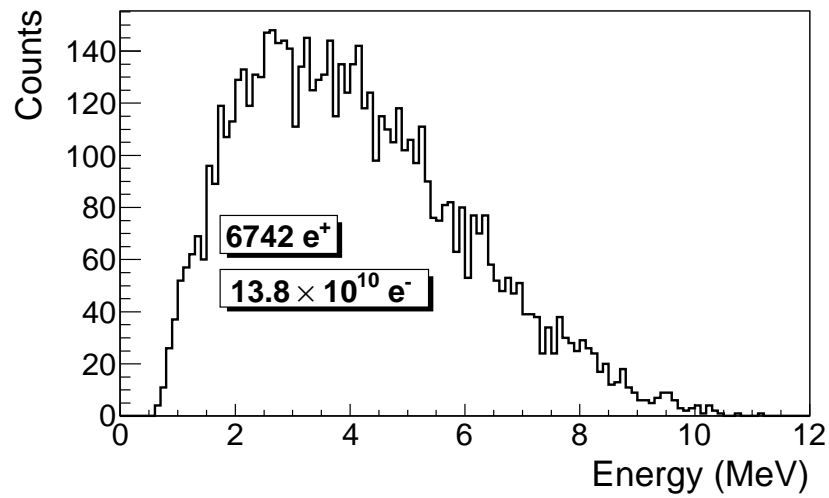
(b) The positron energy distribution on DD1.

Figure 3.6: The positron beam energy distribution detected downstream of T1.
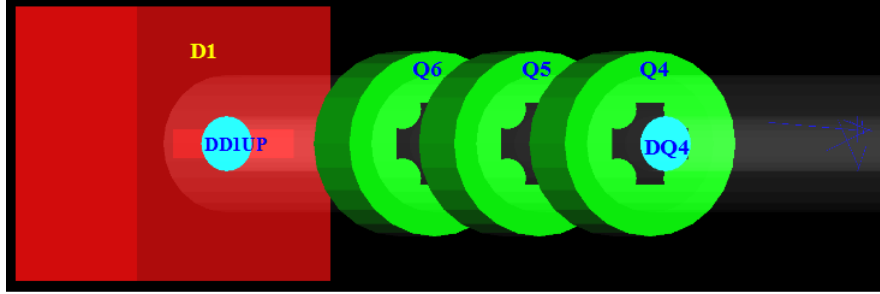
Figure 3.7: The generation and transportation of the positron beam in step 2. The virtual detectors were used to track the positrons.

3.3 Step 3 - The Transportation of Positrons from the Entrance of The First Dipole to T2 and The Detection of 511 keV Photons

In this step, the positron beam was generated at the entrance of the first dipole (DD1UP). The beam was bent 90° by two dipoles and transported to the annihilation target T2 located at the end of the beamline as shown in Figure 3.8.
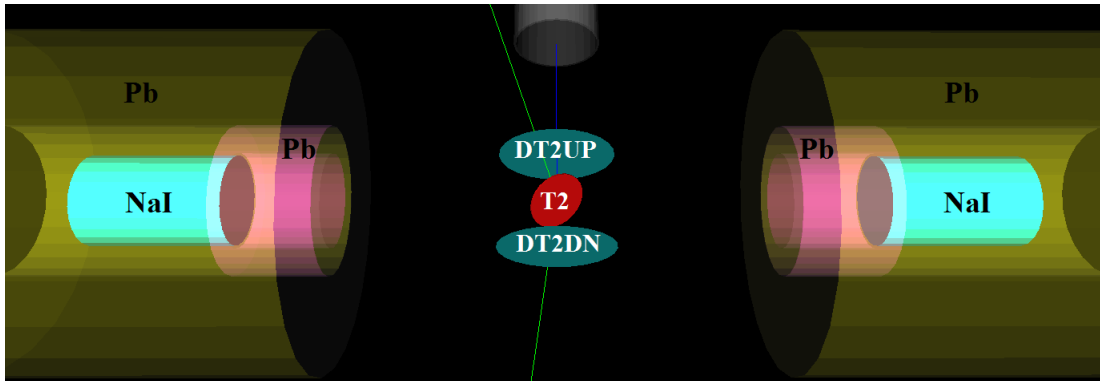
Figure 3.8: T2 and virtual detectors located upstream (DT2UP) and downstream (DT2DN) of T2 are shown at the center of the figure. NaI detectors and Pb shielding are located horizontally at two sides.

As shown in Figure 3.8, two virtual circular detectors DT2UP and DT2DN with a 48 mm diameter (48 mm is the inner diameter of the beam pipe) were placed upstream and downstream of T2 to detect positrons. Two other detector DUPT2 and DDNT2 with the same

diameters as T2 were placed parallel to T2 at two ends of T2 to detect positrons. Two NaI virtual detectors were placed horizontally 170 mm away from the beamline center to detect photons. Two inch thick Pb bricks with 2-inch diameter circular openings faced T2 and surrounded the NaI detectors. When a positron annihilates inside T2, two back-to-back scattered 511 keV photons are generated. An event is registered in the simulation when both NaI detectors observe a 511 keV photon.

3.3.1 Positrons Detected by The Detection System

The detector efficiency chart shown in Figure 3.9, obtained from SAINT-GOBIAN CRYSTALS [19], indicates the NaI crystal has an efficiency of 68% for 511 keV photons. If two detectors are operated in coincidence mode, the detection efficiency of the system is $68\% \times 68\% = 46.24\%$. Figure 3.10 shows the counts of 511 keV photon pairs detected in coincidence mode (multiplied to 46.24%) and overlaid with the positrons that are detected on DDNT1.

3.3.2 Beam Loss Study

The positron distribution observed after T1 was used to send a sample of positrons towards the dipole D1 that would be used to create a positron event generator at the entrance to dipole D1. This procedure was repeated at D1 in order to generate a large positron sample at the annihilation target (T2). This three step procedure reduced the simulation time to generate large positron samples. 7.253×10^{16} electrons incident on the T1 created 5.756×10^{13} positrons as shown in Column 2 in Table 3.1. Columns 2 and 3 in Table 3.1 represent the number of positrons that would need to be generated in order to observe the number of positrons in the remaining columns. The number of 511 keV photon pairs detected by NaI detectors in coincidence mode are shown in the last column of Table 3.1. The number of positrons observed by virtual detectors placed along the beamline and 511 keV photon pairs detected are shown in Figure 3.11.
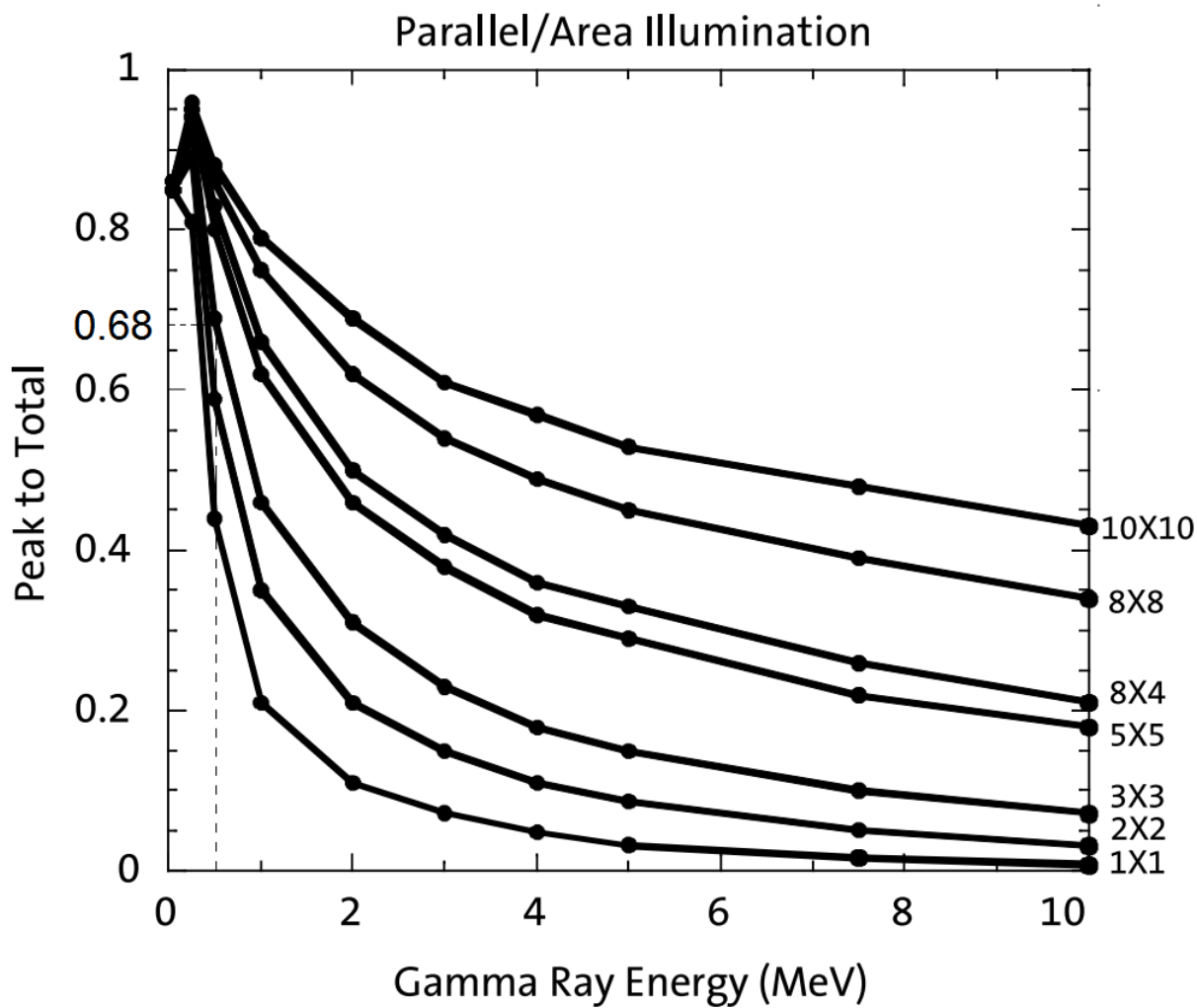
Figure 3.9: NaI detector efficiency obtained from SAINT-GOBIAN CRYSTALS [19]. The lines correspond to the different crystal sizes (in inches)shown on the right side of the figure.

Table 3.1: Predicted Number of Positrons Transported and The Number of 511 keV Photons Detected.

Energy (MeV)	On DDNT1	Enter Q4	Enter D1	Exit D1	Enter Q7	Enter D2	Exit D2	Reach T2	γ on NaI
1.02 ± 0.25	2.5×10^{12}	1.4×10^{10}	1.4×10^{9}	1.2×10^{8}	2.6×10^{7}	2.7×10^{6}	1.2×10^{6}	4.3×10^{3}	7
1.50 ± 0.25	4.9×10^{12}	2.8×10^{10}	2.8×10^{9}	1.8×10^{8}	9.1×10^{7}	2.7×10^{7}	1.2×10^{7}	5.1×10^{4}	97
2.15 ± 0.25	6.5×10^{12}	3.8×10^{10}	3.8×10^{9}	3.8×10^{8}	1.7×10^{8}	7.8×10^{7}	3.6×10^{7}	4.4×10^{5}	734
2.50 ± 0.25	6.8×10^{12}	4.1×10^{10}	4.1×10^{9}	4.4×10^{8}	2.3×10^{8}	1.1×10^{8}	5.0×10^{7}	4.6×10^{5}	794
3.00 ± 0.25	6.6×10^{12}	4.1×10^{10}	4.1×10^{9}	4.6×10^{8}	2.7×10^{8}	1.3×10^{8}	6.1×10^{7}	4.5×10^{5}	723
3.50 ± 0.25	6.1×10^{12}	3.9×10^{10}	3.9×10^{9}	4.4×10^{8}	2.8×10^{8}	1.4×10^{8}	6.7×10^{7}	4.4×10^{5}	716
4.02 ± 0.25	5.3×10^{12}	3.5×10^{10}	3.5×10^{9}	4.1×10^{8}	2.7×10^{8}	1.4×10^{8}	6.9×10^{7}	4.3×10^{5}	702
4.50 ± 0.25	4.6×10^{12}	3.1×10^{10}	3.1×10^{9}	3.6×10^{8}	2.5×10^{8}	1.3×10^{8}	6.7×10^{7}	4.0×10^{5}	646
5.00 ± 0.25	3.8×10^{12}	2.7×10^{10}	2.7×10^{9}	3.1×10^{8}	2.2×10^{8}	1.2×10^{8}	6.2×10^{7}	3.6×10^{5}	566
5.50 ± 0.25	3.0×10^{12}	2.2×10^{10}	2.2×10^{9}	2.6×10^{8}	1.9×10^{8}	1.0×10^{8}	5.6×10^{7}	3.3×10^{5}	533
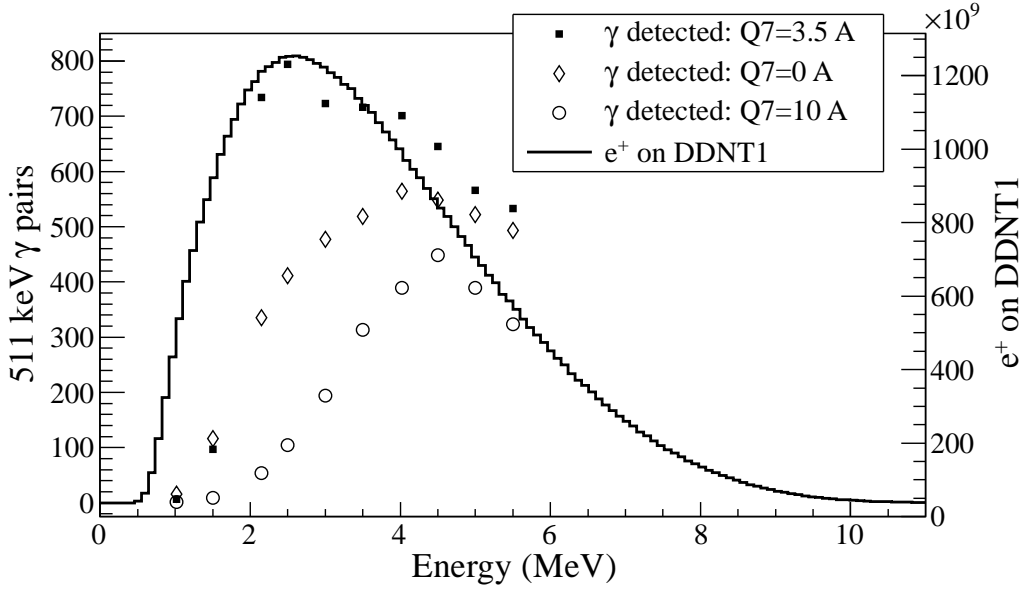
Figure 3.10: Positrons detected on virtual detector DDNT1 and 511 keV photon pairs detected by the NaI detectors in coincidence mode when Q7 is at 0 A, 3.5 A and 10 A.

As shown in Table 3.1, the positron energy distribution is divided into 10 bins. At detector DDNT1 (25.8 mm after T1), there are about 10^{12} positrons in each bin. At the entrance of Q4, the number of positrons dropped two orders of magnitude. This may be attributed to the solid angle that the entrance of Q4 makes with respect to T1, if one assumes T1 is a point source of positrons. The distance between T1 and the virtual detector DQ4 is 560 mm and the radius of DQ4 is 24 mm. The solid angle of the DQ4 is $\Omega_{Q4} = \frac{\pi r^2}{d^2} = \frac{\pi 24^2}{560^2}$ rad. Positrons make up a cone with a 45° half angle, which is $\Omega_{beam} = 0.6\pi$ rad in solid angle. The ratio of the two solid angles, $\Omega_{Q4}/\Omega_{beam}$, is 1:160, $i.e.$ 1 out of 160 positrons make it from T1 to DQ4, assuming that the positron beam is isotropic inside the cone. However, the positron beam peaks at a smaller angle as shown in Figure 3.3 (c) and (d) and as a result more positrons are transported from DDNT1 to DQ4, resulting in a ratio closer to 1:100.

As an example to explain the beam loss along the beamline, in a similar simulation as in Table 3.1, the dipoles were set to transport 3 MeV positrons as shown in Figure 3.12 (Note: One tenth of the particles are plotted because of the large file size) and Table 3.2. The beam
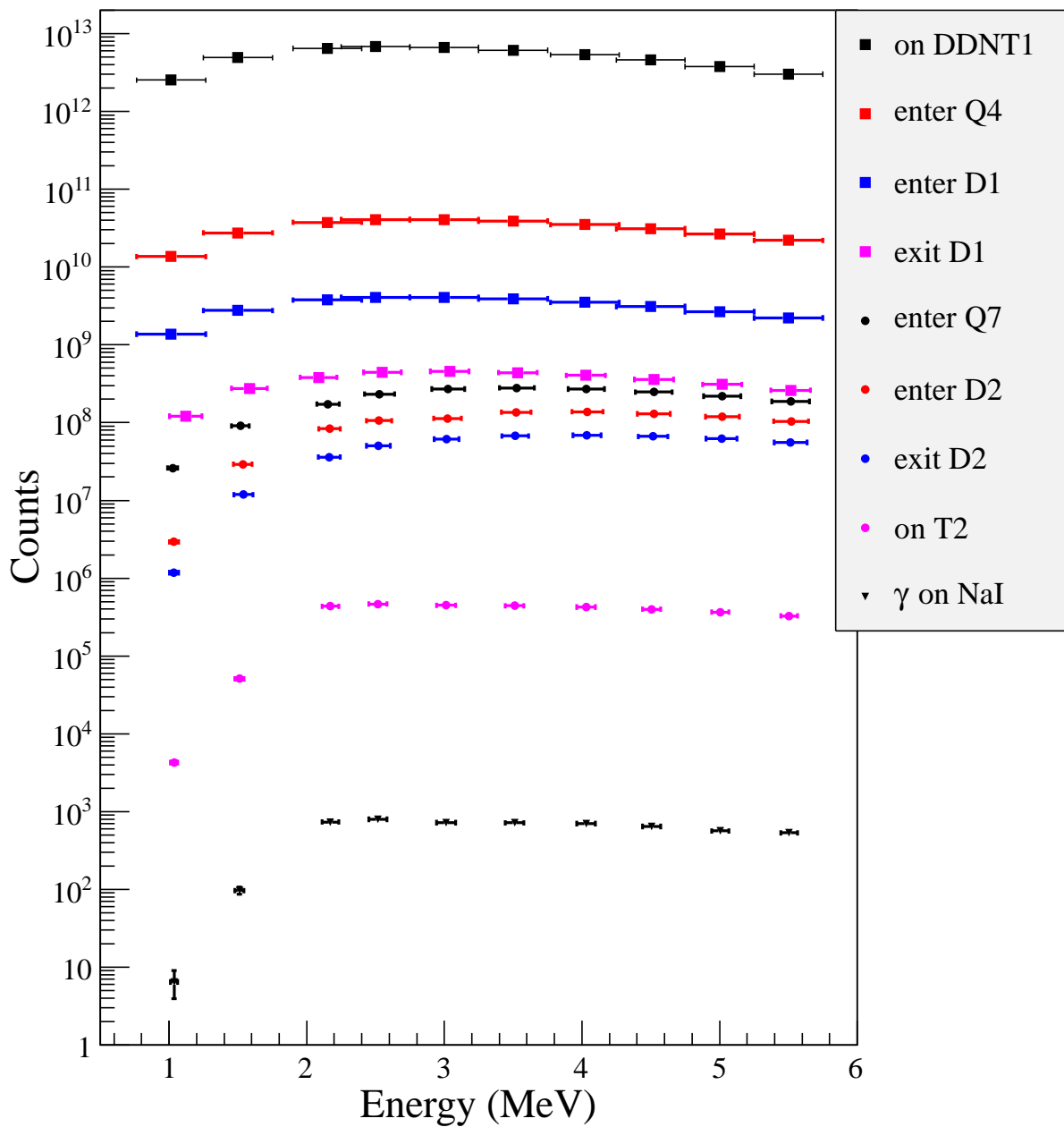
Figure 3.11: Predicted number of positrons transported. Black cube: positrons incident on DDNT1. Red cube: positrons entered Q4. Blue cube: positrons entered D1. Magenta cube: positrons exited D1. Black circle: positrons entered Q7. Red circle: positrons entered D2. Blue circle: positrons exited D2. Magenta circle: positrons incident on DT2UP. Black triangle: 511 keV photons detected by NaI detectors in coincidence mode.

Table 3.2: The Positron Beam Loss Along The Beamline.

Locations The Beam Sampled	Absolute Counts	Relative Counts
e$^+$ on DDNT1	6.6×10^{12}	9.4×10^{10}
e$^+$ enter Q4	4.1×10^{10}	5.8×10^{7}
e$^+$ enter D1	4.1×10^{9}	5.8×10^{6}
e$^+$ exit D1	4.6×10^{8}	6.6×10^{5}
e$^+$ enter Q7	2.7×10^{8}	3.8×10^{5}
e$^+$ enter D2	1.3×10^{8}	1.9×10^{5}
e$^+$ exit D2	6.1×10^{7}	8.7×10^{4}
e$^+$ on T2	4.4×10^{5}	6.3×10^{2}
e$^+$ annihilated in T2	2.5×10^{5}	3.6×10^{2}
511 keV photons on NaI	723	1

energy distribution was plotted at the exit of D1, entrance of Q7, exit of Q7, entrance of D2, exit of D2, and at T2. In Table 3.2, the numbers given in the last column are the relative counts and obtained by dividing the second column by 723, the number of 511 keV photons detected by NaI detectors in coincidence mode.

The distance between NaI detectors and the beamline center is 170 cm. The Pb shielding has a hole facing T2 with a 2 inch diameter. Assuming positrons annihilated at the center of T2, the solid angle made by a NaI detector is $\Omega = \frac{\pi r^2}{d^2} = \frac{\pi 25.4^2}{170^2}$ rad. The 511 keV photons created during the annihilation make a solid angle of 2π rad considering each side of T2 is facing one detector. The ratio of 2π rad to solid angle of T2 is about 90:1.

In a simulation with similar settings as in Table **??**, dipoles were set to bend 3 MeV positrons. 4.4×10^5 positrons were transported to annihilation target T2 and created 254864 511 keV photon pairs (*i.e.* 58% of the positrons annihilated). Two 0.0254 mm thick stainless steel vacuum windows are placed 9 cm from T2 on both sides of the beamline. Detectors are placed in the front and back of vacuum windows to observe their affect on the photons (the detectors are placed 1 μm from the windows). 4330 511 keV photons went into the vacuum window and 4300 made it through. 0.7% of photon pairs are lost when passing through the vacuum windows.

The left NaI detector detected 2897 511 keV photons and the right one detected 4100. The ratio of 511 keV photon pairs created in T2 to those that made it to the right and the left NaI are 88:1 and 62:1 respectively. These are close to the ratios predicted by the solid angle ratio 90:1. 1518 511 keV photon pairs are detected by NaI detectors in coincidence mode. The ratio 511 keV of photon pairs created to the ones detected in coincidence mode is 168:1. Counting photons in coincidence mode cut the rate by half. Note that these counts are given after considering detection efficiency of the system.
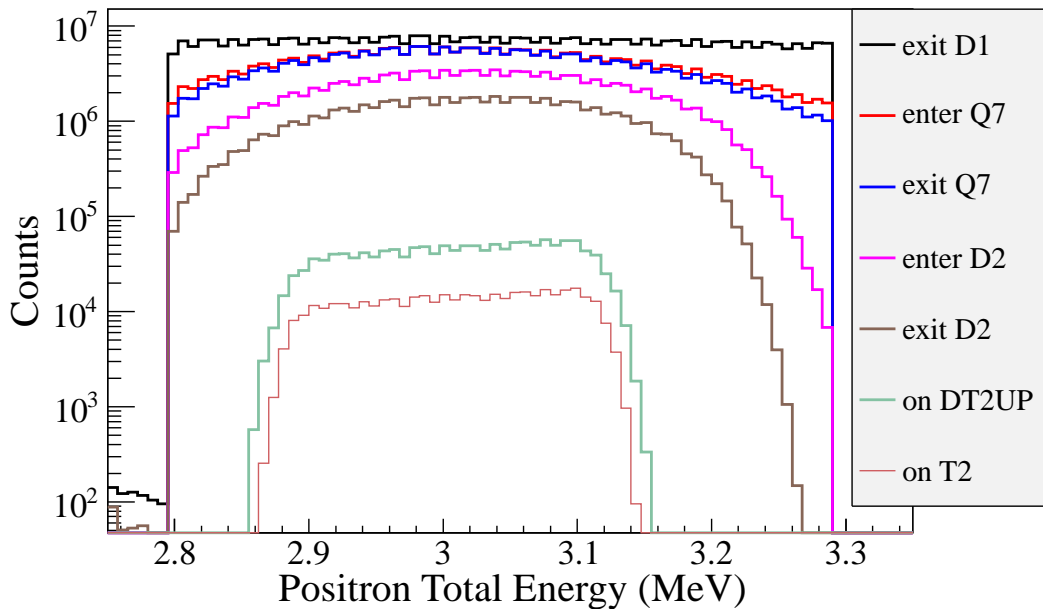
Figure 3.12: Positrons transported when dipoles are set to bend 3 MeV positrons.

3.4 Quadrupole Triplet Collection Efficiency Study

In this simulation, 5,475,869,400 positrons were generated at DDNT1 and transported to DD1 to study quadrupole triplet positron collection and transportation efficiency. Six quadrupole current settings of the triplet system were simulated as shown in Table 3.3. For different quadrupole current settings, no significant differences were observed in the number of positrons, transverse beam profiles and momentum distributions. The ratio of positrons

generated at DDNT1 to the ones that enter D1 is 1525:1.

3.5   Error Study

Systematic errors in positron counts were estimated by carrying out simulations with different magnet settings as shown in Table 3.4. The magnet settings are indicated in top 3 rows of Table 3.4. The energy of positrons being transported are given in the first column. The 511 keV photon pairs counted in coincidence mode (*i.e.* the original counts was multiplied by 46.42%) for different magnet settings are given in the corresponding columns below.

The uncertainty of the magnet power supply is 0.1 A. The Max/Min in the table refers to the Maximum/Minimum magnetic filed strength when the magnet coil current is at $I_{\max}/I_{\min}$, where $I_{\max} = I_{\text{def}} + 0.1$ A and $I_{\min} = I_{\text{def}} - 0.1$ A. Def refers to the default magnetic field strength of the magnet.

The average counts and fractional errors are shown in the last two columns of Table 3.4. The fractional error in the 511 keV photon pair counts is calculated by dividing the standard deviation of counts by the counts in default magnet setting, *i.e.* $\frac{\text{standard deviation of counts}}{\text{counts in defalt setting}}$.

Table 3.3: Quadrupole Triplet System Collection and Transportation Efficiency Data.

Q4	Q5	Q6	Entries	x	σ_x	y	σ_y	P_x	σ_{P_x}	P_y	σ_{P_y}	P_z	σ_{P_z}
A	A	A		mm	mm	mm	mm	MeV	MeV	MeV	MeV	MeV	MeV
-1	2	-1	3587220	-0.005	12	0.030	12	3.0×10^{-5}	0.0461	-0.00216	0.04553	3.848	1.875
-2	4	-2	3591423	-0.012	12	0.049	12	2.2×10^{-5}	0.0461	-0.00211	0.04554	3.848	1.875
1	-2	1	3591509	-0.009	12	0.040	12	-1.5×10^{-5}	0.0462	-0.00216	0.04557	3.849	1.876
1	2	1	3589854	-0.005	12	0.034	12	-1.8×10^{-5}	0.0462	-0.00216	0.04556	3.849	1.876
2	-4	2	3592977	-0.007	12	0.032	12	-3.3×10^{-6}	0.0462	-0.00217	0.04549	3.849	1.876
2	4	2	3589495	-0.004	12	0.033	12	3.0×10^{-6}	0.0462	-0.00218	0.04554	3.849	1.875

Table 3.4: Systematic Error Study: Counts of 511 keV Photon Pairs for Different Magnet Settings.

D1	Max	Min	Max	Min	Max	Max	Min	Min	Def		
Q7	Def	Def	Def	Def	Max	Min	Min	Def	Def		
D2	Max	Min	Def	Def	Def	Def	Def	Def	Def	Average	Fractional Error
Energy (MeV)											
0.765 1.265	12	2	3	1	1	3	3	0	6	4	57.3 %
1.25 - 1.75	95	75	70	86	85	92	129	86	97	90	17.6 %
1.85 - 2.35	674	724	737	769	686	747	803	681	734	728	5.8 %
2.25 - 2.75	781	755	753	759	772	963	794	763	794	793	8.3 %
2.75 - 3.25	739	737	765	752	738	698	738	757	723	739	2.7 %
3.25 - 3.75	713	699	747	712	707	751	718	705	716	719	2.5 %
3.77 - 4.27	690	708	715	676	704	658	706	715	701	697	2.7 %
4.25 - 4.75	627	666	634	646	635	675	637	653	646	646	2.5 %
4.75 - 5.25	558	595	594	603	606	688	582	582	566	597	6.7 %
5.25 - 5.75	513	536	535	522	525	535	518	544	533	529	1.9 %

Chapter 4

Experiment

4.1   Quadrupole Scanning Experiment

Quadrupole scanning method was used to measure the accelerator's emittance. The quadrupole current is changed to alter the strength and direction of the quadrupole magnetic field such that a measurable change in the beam shape is seen by the OTR system. Initially, the beam was steered by the quadrupole indicating that the beam was not entering along the quadrupole's central axis. Several magnetic elements upstream of this quadrupole were adjusted to align the incident electron beam with the quadrupole's central axis. First, the beam current observed by a Faraday cup located at the end of beam line was maximized using upstream steering coils within the linac nearest the gun. Second, the first solenoid nearest the linac gun was used to focus the electron beam on the OTR screen. Steering coils were adjusted to maximize the beam current to the Faraday cup and minimize the deflection of the beam by the quadrupole. A second solenoid and the last steering magnet shown in Figure 2.1, both near the exit of the linac, were used in the final step to optimize the beam spot size on the OTR target and maximize the Faraday cup current. A configuration was found that minimized the electron beam deflection when the quadrupole current was altered during the emittance measurements.

The emittance measurement was performed using an electron beam energy of 15 MeV and a 200 ns long macro pulse of 40 mA current. The current in the first quadrupole after the exit of the linac was changed from -5 A to $+5$ A with an increment of 0.2 A. Seven measurements were taken at each current step in order to determine the average beam width and the variance. Background measurements were taken by turning the linac's electron gun

off while keep the RF on. Background image and beam images before and after background subtraction are shown in Figure 4.1. A small dark current is visible in Figure 4.1 (b) that is known to be generated when electrons are pulled off the cavity wall and accelerated.

The electron beam energy was measured using a dipole magnet downstream of the quadrupole used for the emittance measurements. Prior to energizing the dipole, the electron micro-pulse bunch charge passing through the dipole was measured using a Faraday cup located approximately 50 cm downstream of the OTR screen. The dipole current was adjusted until a maximum beam current was observed on another Faraday cup located just after the 45 degree exit port of the dipole. A magnetic field map of the dipole indicates that the electron beam energy was 15 ± 1.6 MeV.

Images from the JAI camera were calibrated using the OTR target frame. An LED was used to illuminate the OTR aluminum frame that has a known inner diameter of 31.75 mm. Image processing software was used to inscribe a circle on the image to measure the circular OTR inner frame in units of pixels. The scaling factor can be obtained by dividing this length with the number of pixels observed. The result is a horizontal scaling factor of 0.04327 ± 0.00016 mm/pixel and vertical scaling factor of 0.04204 ± 0.00018 mm/pixel. Digital images from the JAI camera were extracted in a matrix format in order to take projections on both axes and perform a Gaussian fit. The observed image profiles were not well described by a single Gaussian distribution.

The profiles may be described using a Lorentzian distribution, however, the rms of the Lorentzian function is not defined. A super Gaussian distribution was used [20], because it has a sharper distribution than Gaussian and unlike Lorentzian the rms values may be directly extracted. The Chi-square per degree of freedom for x and y profiles are 3.1×10^4 and 3.3×10^4 for super Gaussian fit and 3.4×10^5 and 1.6×10^5 Gaussian fit. The beam spot, beam projections and fits are shown in Figure 4.2. In Gaussian distribution, $\phi(x) = \frac{1}{\sqrt{2\pi}} e^{-\frac{1}{2}x^2}$, the variable x on exponent is raised to the 2nd power while in the super Gaussian it is raised to a power smaller than 2. For example, the beam projections shown in Figure 4.2 were fitted with the super Gaussian distributions. The variable x on exponents were raised to 0.9053
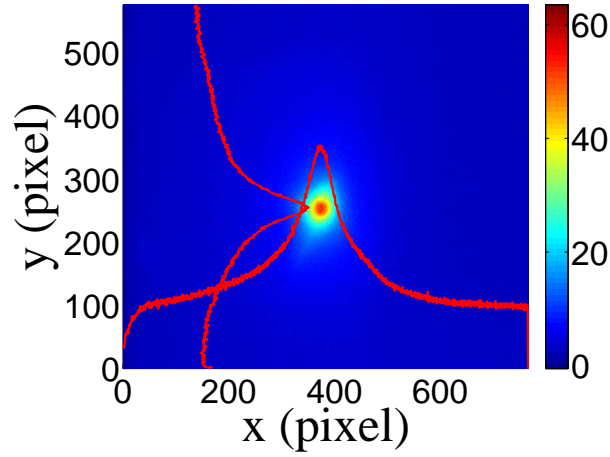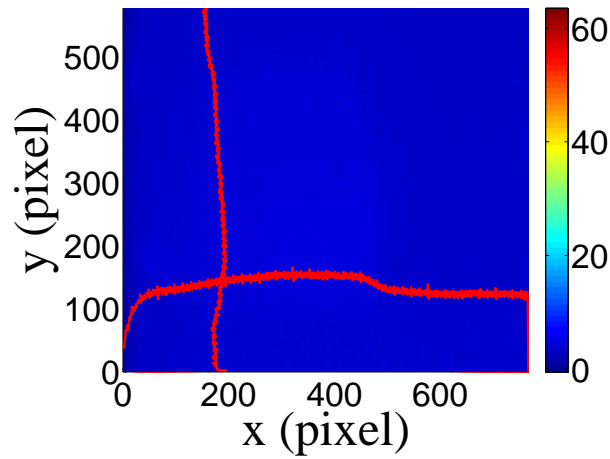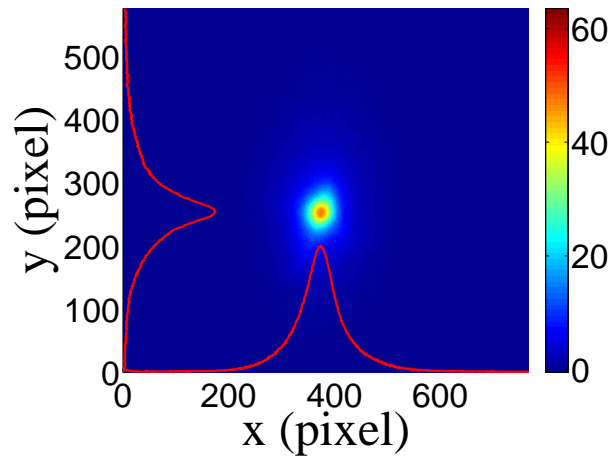
Figure 4.1: Digital image from the OTR screen; (a) a beam with the dark current and background noise, (b) a background image taken after the RF was on but the gun is off, (c) a beam image when dark background was subtracted.

(x-projection) and 1.0427 (y-projection).
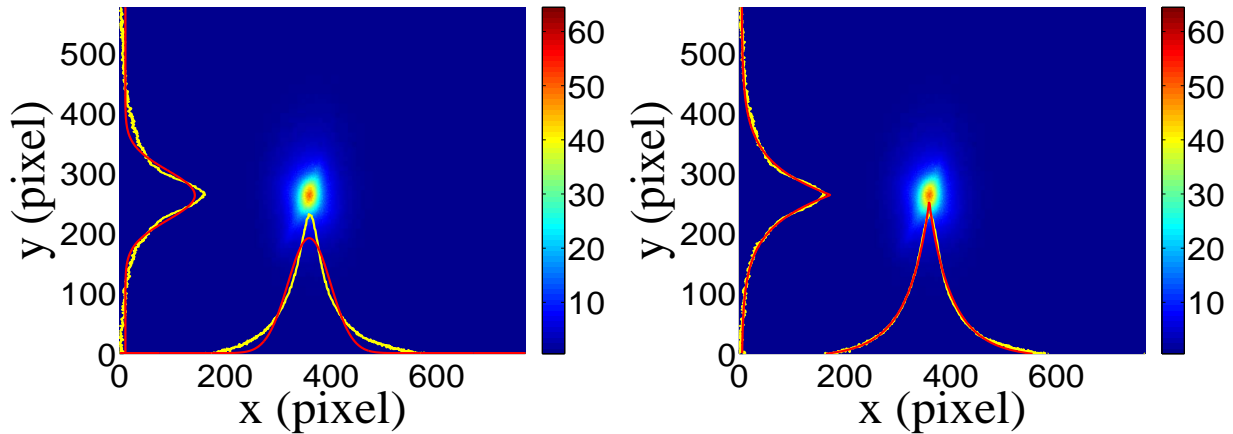
Figure 4.2: Gaussian and super Gaussian fits for beam projections. The beam images is background subtracted image and taken when quadrupole magnets are turned off. Left image is Gaussian fit and right image is super Gaussian fit.

Figure 4.3 shows the square of the rms (σ_s^2) vs k_1L for x (horizontal) and y (vertical) beam projections along with the parabolic fits using Eq. 4.3. The emittance and Twiss parameters from these fits are summarized in Table 4.1. MATLAB scripts used to calculate emittance and Twiss parameters are given in appendix B.
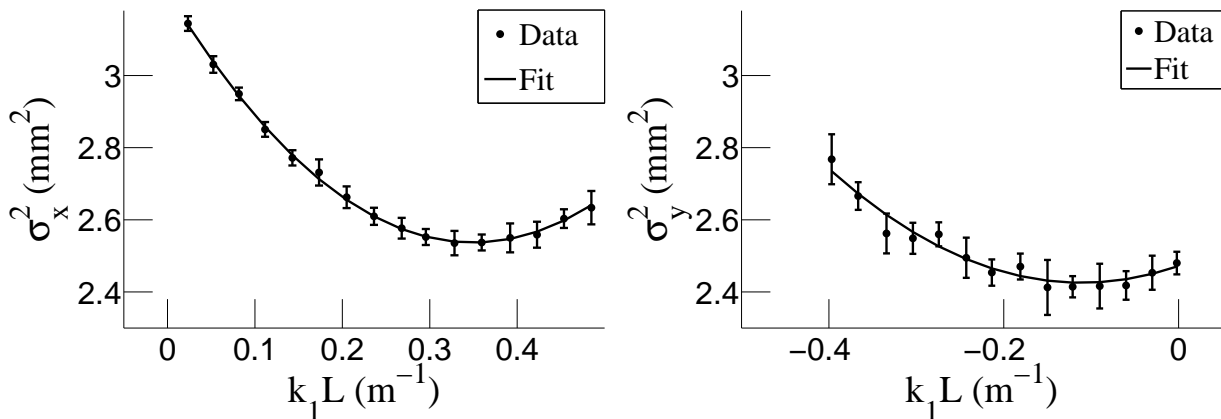
Figure 4.3: Square of rms values and parabolic fittings.

Table 4.1: Emittance Measurement Results

Parameter	Unit	Value
projected emittance ϵ_x	μm	0.37 ± 0.02
projected emittance ϵ_y	μm	0.30 ± 0.04
β_x-function	m	1.40 ± 0.06
β_y-function	m	1.17 ± 0.13
α_x-function	rad	0.97 ± 0.06
α_y-function	rad	0.24 ± 0.07
micro-pulse charge	pC	11
micro-pulse length	ps	35
energy of the beam E	MeV	15 ± 1.6
relative energy spread $\Delta E/E$	%	10.4

4.2 Energy Scan

The HRRL energy profile was measured when it was tuned to accelerate electrons to 12 MeV peak energy. A Faraday cup was placed at the end of the 45 degree beamline to measure the electron beam current when D1 was on and D2 was off. Dipole coil current for D1 was changed in 1 A increments. As the dipole coil current was changed, the energy of the electrons transported to the Faraday cup would change as described in Appendix A. Figure 4.4 illustrates a measurement of the 12 MeV peak with a long low energy tail observed. The HRRL energy profile can be described by overlapping two skewed Gaussian fits [20]. The fit function is given by

$$G(En) = A_1 e^{\frac{-(En-\mu_1)^2}{2\{\sigma_1[1+sgn(En-\mu_1)]\}^2}} + A_2 e^{\frac{-(En-\mu_2)^2}{2\{\sigma_2[1+sgn(En-\mu_2)]\}^2}}, \tag{4.1}$$

where sgn is the sign function, that is defined as

$$sgn = \begin{cases} -1 & (x < 0) \\ 0 & (x = 0) \\ 1 & (x > 0). \end{cases}$$

48

Table 4.2: Fit Parameters for Two Skewed Gaussian.

Parameter	Notation	Unit	First Gaussian	Second Gaussian
amplitude	A	mA	2.14	10.88
mean	μ	MeV	12.07	12.32
sigma left	σ_L	MeV	4.47	0.70
sigma right	σ_R	MeV	1.20	0.45

Where other variables defined as $\sigma_1 = \frac{\sigma_{r,1}+\sigma_{l,1}}{2}$, $\sigma_2 = \frac{\sigma_{r,2}+\sigma_{l,2}}{2}$, $E_1 = \frac{\sigma_{r,1}-\sigma_{l,1}}{\sigma_{r,1}+\sigma_{l,1}}$, and $E_2 = \frac{\sigma_{r,2}-\sigma_{l,2}}{\sigma_{r,2}+\sigma_{l,2}}$. The measurement results and fits are shown in Figure 4.4 and in Table 4.2.
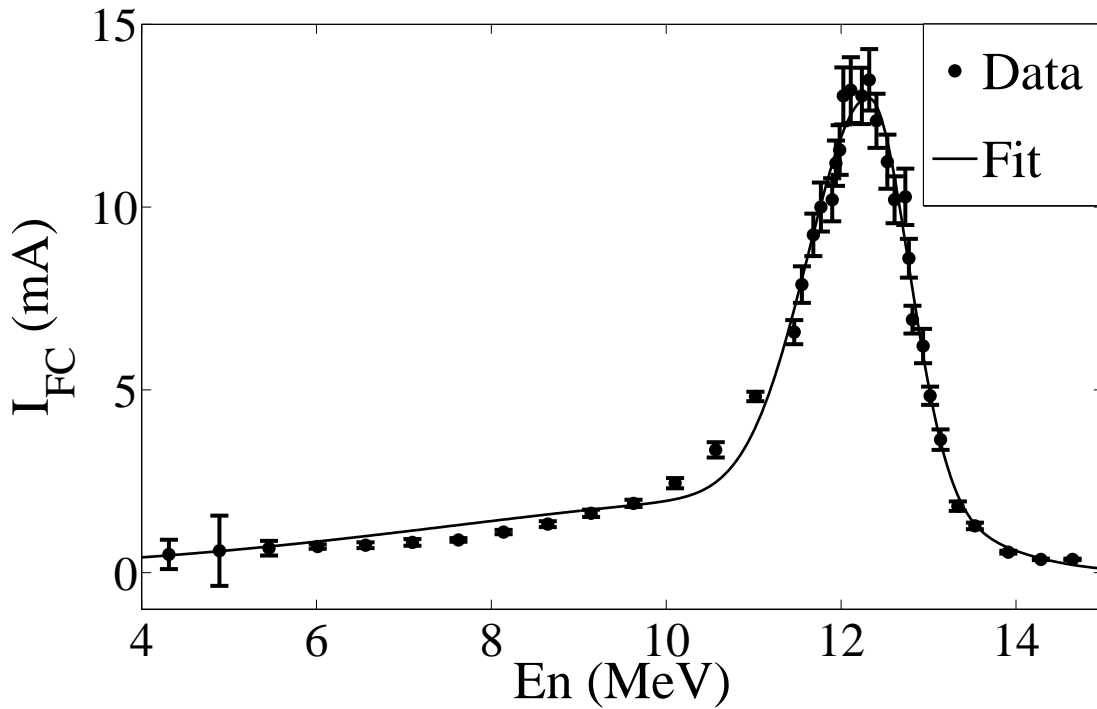
Figure 4.4: HRRL energy scan (dots) and fit (line) with two skewed Gaussian distribution.

4.3   The Positron Production Runs

The annihilation target T2 is insertable into the beamline and it was placed inside a 6-way cross that has horizontal sides sealed with 1 mil stainless steel windows. Positrons intercepting T2 thermalize, annihilate, and produce 511 keV photon pairs back-to-back.

These photons are detected by two NaI detectors facing T2 and shielded with Pb bricks
as shown in Figure 4.5. The background was measured by retracting T2 thereby allowing
positrons to exit the beamline and be absorbed by the beam dump.
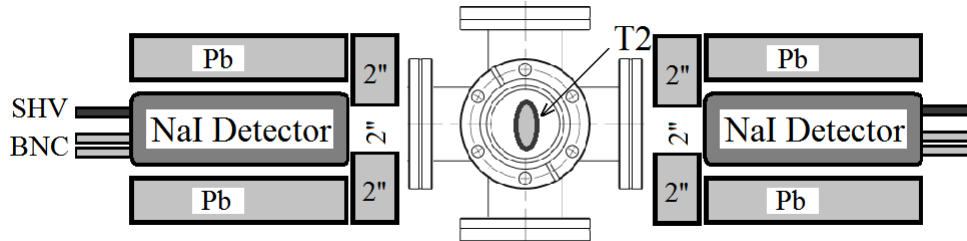
Figure 4.5: Positron detection using T2 and NaI detectors.

As shown in Figure 4.6, a 511 keV peak was observed (solid line) when T2 was in. A
permanent dipole magnet was placed on the beamline after Q10 to deflect charged particles
on the accelerator side preventing them from entering the shielded cell. The peak was not
observed (dashed line) when T2 was in and the permanent magnet was used. The peak was
also not observed (doted dashed line) when T2 and the permanent magnet were removed.
Thus, one may argue that the observed peak is due to positrons annihilating in T2.
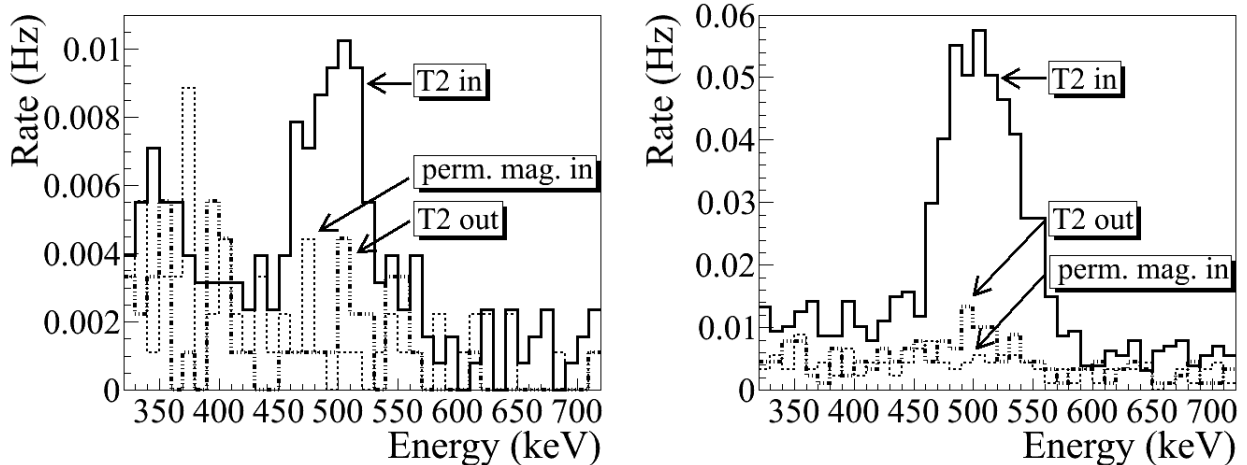
(a) Original spectrum on left NaI.

(b) Original spectrum on right NaI.

Figure 4.6: Photon spectrum when a permanent dipole magnet is inserted along with T2
(dashed line), dipole out and T2 in (solid line), and dipole removed and T2 out (dotted
dashed line). The positron energy incident on the T2 was 2.15 ± 0.06 MeV.

Table 4.3: Scintillator Calibration Data.

Run Number	Faraday Cup Charge Area (nVs)	Mean of ADC Channel 9
3703	1201 ± 10	1126 ± 0.8
3705	777 ± 110	791.8 ± 0.6
3706	367.7 ± 2.3	242.1 ± 0.3

The normalized photon energy spectra observed by two NaI detectors are shown in Figure 4.7 when T2 was both in (signal) and out (background) of the beamline. Figure 4.7 (c) and (d) illustrate the events observed when 511 keV photons were required in both detectors. The signal is indicated by the solid line and background by dashed line.

4.4   The Electron Beam Current Measurement

A scintillator was placed between Q9 and Q10, as shown in Figure 4.8, to monitor the electron beam current. The electron beam current was changed incrementally to measure the correlation between the scintillator and the accelerated electron beam. The beam current was measured using FC1 and the output was integrated using an oscilloscope. The scintillator output was measured by integrating the output of FC1 on an oscilloscope. As the electron beam current was decreased, the signal observed on the oscilloscope decreased and ADC measured less charge from the scintillator as shown in Figure 4.9. A linear fit to data resulted a linear relation

$$Q_{e^-}(i) = (0.0186 \pm 0.0028)i + 2.79 \pm 0.08 \text{ C}, \tag{4.2}$$

where i is ADC channel number and Q is the accelerated electron beam charge. The fit is shown in Figure 4.10.

When running in coincidence mode, the electron beam current is sampled by the scintillator only when a coincidence event occurs causing a trigger that gates the ADC and measures
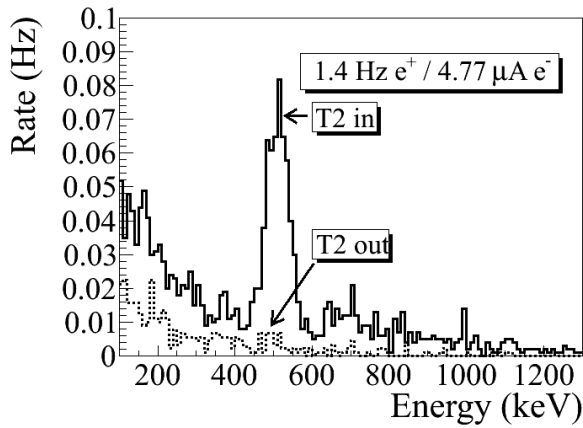
(a) Original spectrum on left NaI.
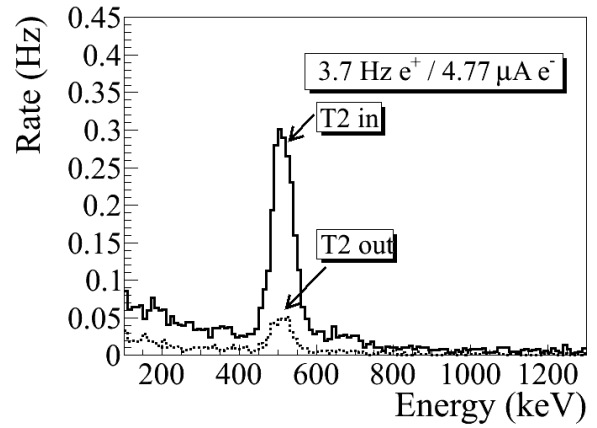
(b) Original spectrum on right NaI.
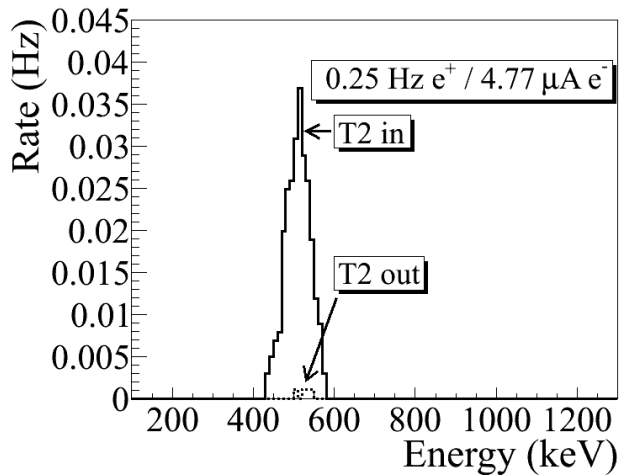
(c) Spectrum with cut on left NaI.
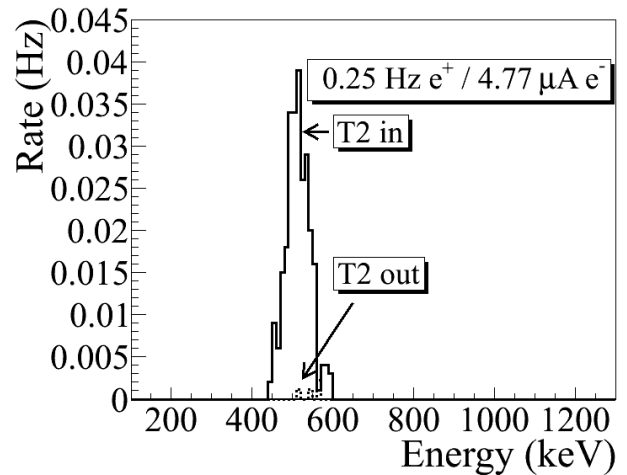
(d) Spectrum with cut on right NaI.

Figure 4.7: The time normalized spectra of photons created by 3 MeV positrons incident on T2. In the top row are original spectrum and in the bottom row are spectrum of incidents happened in the 511 keV peak coincidently in both detectors. The positron beam energy incident on the T2 was 3.00 ± 0.06 MeV.
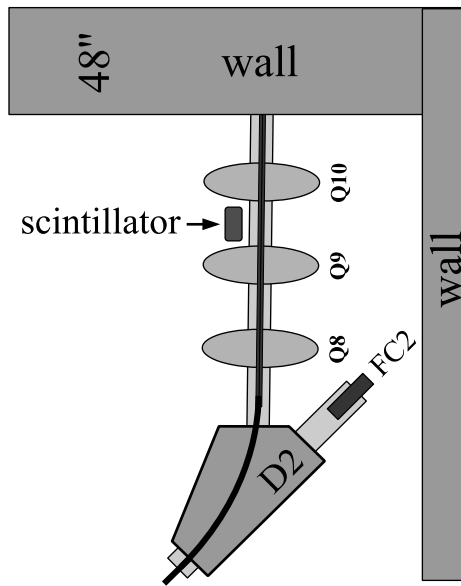
Figure 4.8: The electron beam monitor.
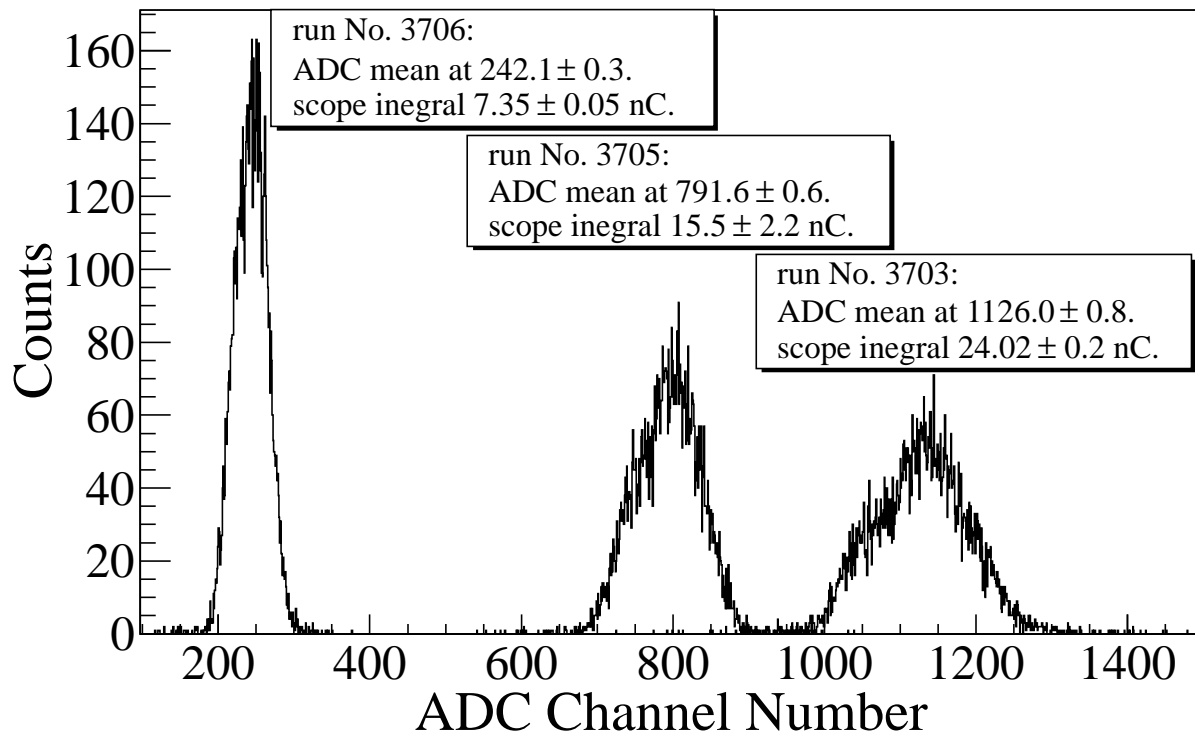
Figure 4.9: The photon flux detected using scintillator. The mean of the ADC channel decreased linearly as the electron beam current was decreased.
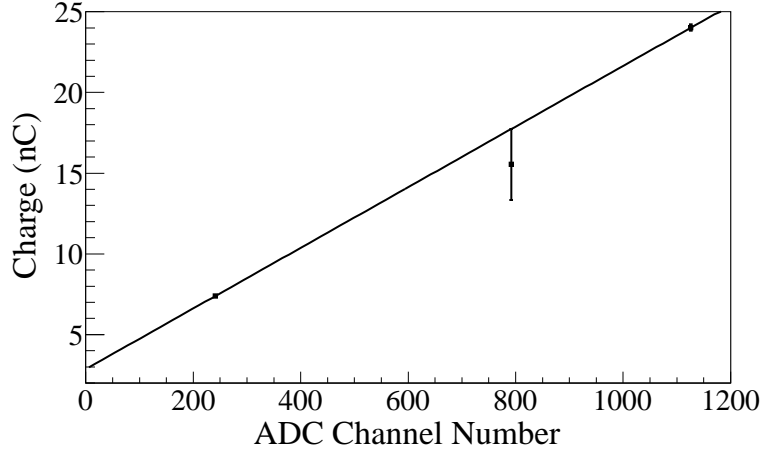
Figure 4.10: Fit for accelerator beam current $v.s.$ the ADC channel.

the scintillator output for that positron coincidence event. The charge measured by the ADC is the total charge of the electron pulses that created the positron events. The beam pulses are counted using a scaler. The total charge on T1 for the entire run is estimated using

$$Q_{\mathrm{C}} = \left(\sum_{i}^{N} 0.0186 i \times (\text{bin content}[i]) + 2.79 \right) \times \frac{(\text{\# of beam pulses})}{(\text{\# of events})}. \tag{4.3}$$

4.5 Positron Rate Estimation in Coincidence Mode

The background subtracted and normalized photon energy spectra were observed using two NaI detectors for 3.00 ± 0.07 MeV are shown in Figure 4.7. Figure 4.7 (a) and (b) are the background subtracted spectrum with no coincidence or energy cut. Figure 4.7 (c) and (d) illustrate events observed in coincidence and within a energy window of 511 ± 75 keV for both detectors. The measured positron rate using NaI detectors in coincidence mode was 0.25 Hz for 3.00 ± 0.07 MeV positrons.
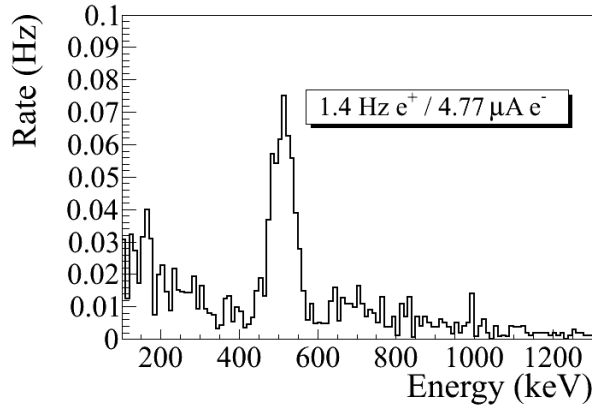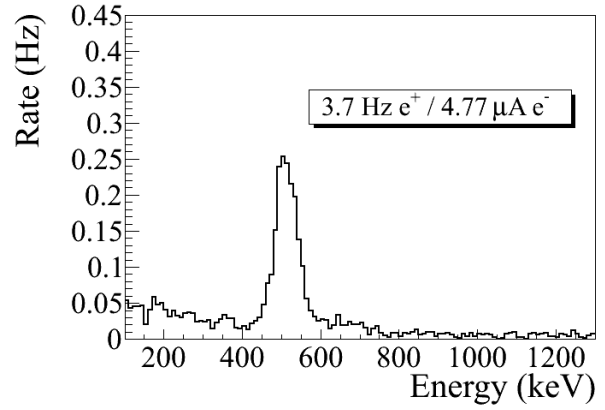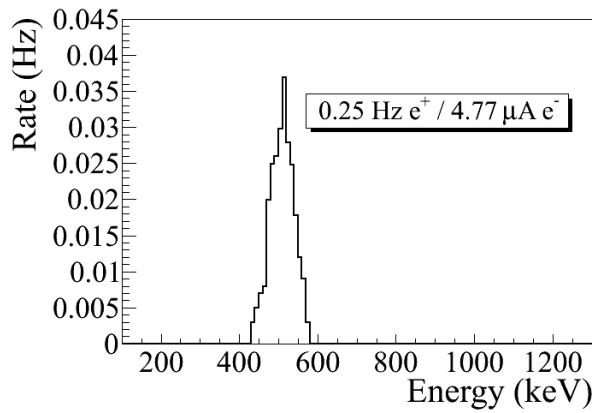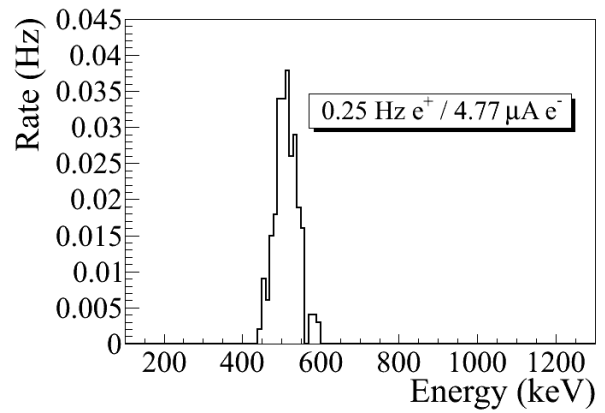
Figure 4.11: Photon spectrum of NaI detectors after background subtraction created by 3 MeV positrons incident on T2. (a) and (b) are spectrum after background subtractions. (c) and (d) are the spectrum of events coincident in both detectors in 511 keV peaks.

4.6 Positron Rate Estimation in OR Mode

The Positron rate was also measured by running NaI detectors in OR mode and the photon spectrum are shown in Figure 4.12 for 2.15 ± 0.06 MeV positrons incident T2. The rate was 0.21 Hz for left and 0.35 Hz right NaI detectors in OR mode while the rate in coincidence (AND) mode was 0.028 Hz.

(a) Left NaI detector.

(b) Right NaI detector.
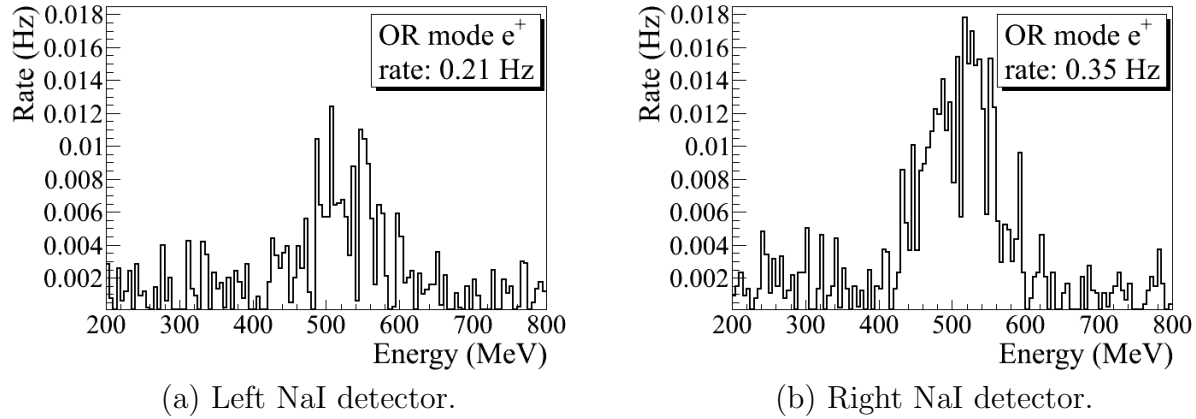
Figure 4.12: The Positron rates were also measured by running NaI detectors in OR mode. The rate was 0.21 Hz for left and 0.35 Hz right NaI detectors in OR mode while the rate in coincidence (AND) mode was 0.028 Hz.

4.7 Positron to Electron Ratio

The ratios of positrons detected using NaI detectors in coincidence mode to the electrons impinging T1 at different energies are given in Table 4.4 and Figure 4.13. A simulation was used to estimate the systematic error of the positrons at different energies. The ratios errors are calculated by propagating the statistical errors of positron and electron rates.

Table 4.4: Positron to Electron Rate Ratio.

Energy	Positron to Electron Ratio
1.02 ± 0.03	$(0.19 \pm 0.19) \times 10^{-16}$
2.15 ± 0.06	$(0.69 \pm 0.24) \times 10^{-16}$
3.00 ± 0.07	$(8.25 \pm 0.96) \times 10^{-15}$
4.02 ± 0.07	$(4.20 \pm 0.80) \times 10^{-15}$
5.00 ± 0.06	$(0.62 \pm 0.16) \times 10^{-16}$
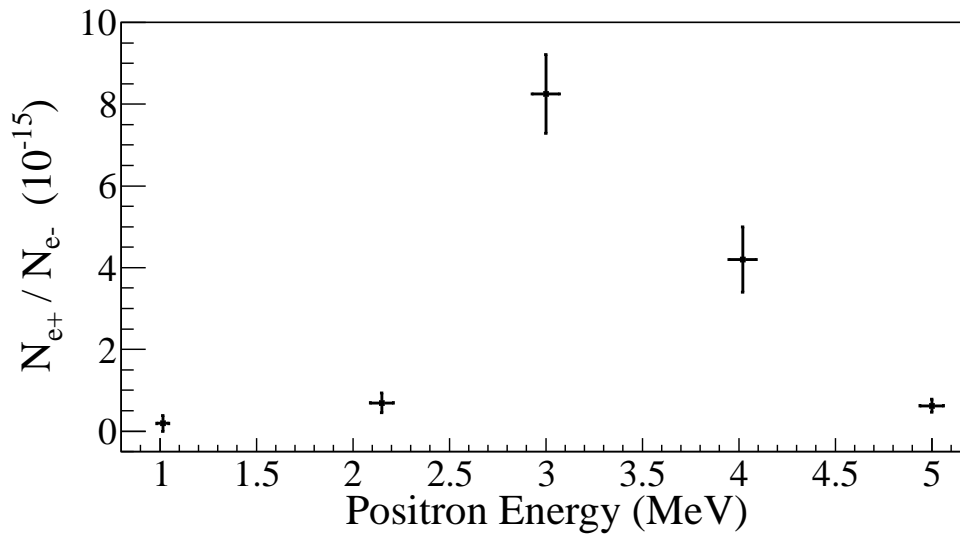
Figure 4.13: The ratios of positrons detected by NaI detectors in coincidence mode to the electrons impinging T1.

Chapter 5

Conclusions and Suggestions

The HRRL cavity was moved to new location to add new magnetic elements and diagnostic tolls to the beamline. The new HRRL beamline had been successfully reconfigured to produce positrons while still can transport electrons to the experimental cell.

An OTR based diagnostic tool was developed and used to measure the beam emittance of the HRRL. The electron beam profile was not described well using a Gaussian distribution but rather by a super Gaussian or Lorentzian distribution. The projected emittances of the HRRL were measured to be less than 0.4 μm as measured by the OTR based tool when accelerating electrons to an energy of 15 MeV.

The positron detection system was successfully constructed using two NaI detectors and the thin tungsten target placed in the 6-way cross. Positrons were measured at different energies $(1 - 5 \text{ MeV})$ in experiment. The ratio of positrons being detected on NaI detectors to electrons incident on T1 is on the order of 10^{-15} and the peak is observed near 3 MeV.

Simulation results indicate that the transportation efficiency varies for different energies. Higher energies positrons were transported with higher efficiency and vise versa. While simulation result agrees with experiment in that the peak energy distribution is near 3 MeV, it predicts higher positron to electron ratio as shown in Figure 5.1.

Experimental results show quadrupole magnets are not efficient in collecting positrons, since positrons have large angular distributions. Solenoid may be better option to improve the collection efficiency of the positrons. Placing the quadrupole (or solenoid) close the production target may increase the positron transportation efficiency since it can capture more positrons.
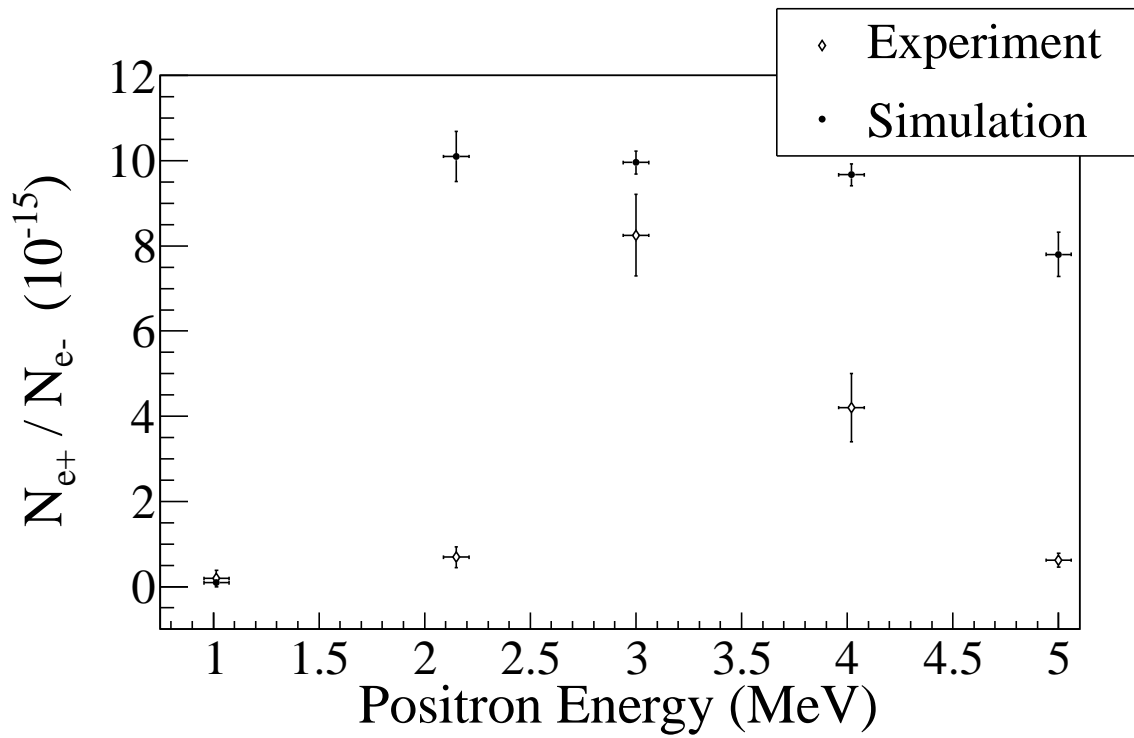
Figure 5.1: Ratio of positrons detected to electrons in experiment and simulation.

Appendix A

The Electron Beam Energy Scan

The electron beam energy was scanned using a dipole magnet. The dipole magnet current was increased incrementally and the electron beam current corresponding to that bent portion of the electron beam was measured with a Faraday cup.

Table A.1: Dipole Magnet Mapping Data.

Dipole Magnet Coil Current (A)	Faraday Cup Current (mA)	Electron Beam Energy (MeV)
8	0.5	4.3119
9	0.6	4.8896
10	0.67	5.4570
11	0.716	6.0141
12	0.752	6.5610
13	0.828	7.0975
14	0.896	7.6238
15	1.112	8.1399
16	1.328	8.6456
17	1.624	9.1411
18	1.896	9.6262
19	2.448	10.1012
20	3.36	10.5658

Continued on next page

Table A.1 – *Continued from previous page*

Dipole Magnet Coil Current (A)	Faraday Cup Current (mA)	Electron Beam Energy (MeV)
21	4.82	11.0201
22	6.58	11.4642
22.2	7.88	11.5518
22.5	9.24	11.6824
22.7	10.0	11.7690
23	10.2	11.8980
23.1	11.2	11.9408
23.2	11.56	11.9836
23.3	13.04	12.0262
23.5	13.2	12.1111
23.8	13.04	12.2377
24	13.48	12.3216
24.2	12.36	12.4050
24.5	11.24	12.5295
24.7	10.2	12.6119
25	10.28	12.7348
25.1	8.6	12.7756
25.2	6.92	12.8162
25.5	6.2	12.9376
25.7	4.84	13.0180
26	3.64	13.1378
26.5	1.82	13.3354
27	1.28	13.5305

Continued on next page

Table A.1 – *Continued from previous page*

Dipole Magnet Coil Current (A)	Faraday Cup Current (mA)	Electron Beam Energy (MeV)
28	0.56	13.9129
29	0.364	14.2850
30	0.364	14.6469

Appendix B

MATLAB Scripts for Calculating Emittance

The main script "Emit_Calc.m" loads and digitize electron beam images. By projecting the 2D beam to the axis, 1D beam profile is extracted and passed to "SupGau_devsum.m" for super Gaussian fitting. "SupGau_devsum.m" returns rms of the super Gaussian fit. The rms values of different images are sent to "Emit_Parabola_Fit_kl_XProjection".

"Emit_Parabola_Fit_kl_XProjection" fits parabola for given rms values, plots the fit and extract the emittance and Twiss parameters from the fit.

B.1   Emittance Calculator

```
% Emit_Calc.m
% Reads images from files and digitize images.
% Fits a super Gaussian funtion on the projection, get the rms values.
% Then pass them to fit parabola
%
% April-2011
% Sadiq Setiniyaz

clc;
clear
```

```matlab
me = 0.511; % electron rest mass in MeV

%En = 14; %enter beam energy here in MeV unit.

En = 14.9985 ; %14.9985 MeV energy at Mar 17th, 2011.

En_er = En*0.1; % Assume 5% error on Energy

L = 0.08; % pole face is 8 cm long in z direction.

R_Bore = 0.0254; %Radius of the Bore aperture = center to pole face = 1 inch.

%L_ef = L + R_Bore;

%I_max_neg = -10; %enter smallest negative scan current. Here -7 Amps

%I_max_pos = 7; %enter biggest positive scan current. Here 10 Amps

I_start=-3.0; % Scan starting current

%I_end=-2.0; % Scan ending current

I_increment=0.2;

scan_current_number=31; % do 13 scan.

scan_times=7;


%for ii = 1:scan_step

%    I(ii) = I_start + (ii-1)*I_increment;

%end


p = sqrt(En*En - me*me)/1000;% e- momentum in GeV/c


%%%%%%%%%%%%%%%%%%%%%%%%%%%%%%%%%%%%%%%%%

% Enter the distance from the center of the quad to the screen

S12=3.1;%(in m unit) S12(q4)=1.875 cm. S12(q1)=3.10 cm

erS12 = 0.005; % assume 51 mm error.

%%%%%%%%%%%%%%%%%%%%%%%%%%%%%%%%%%%%%%%%%%%
```

```matlab
%%%%%%%%%%%%%%%%%%%%%%%%%%%%%%%%%%%%%%%%%%%%%%%%%%%%%%%%%%%%%%
%Enter calibration here:
calibration_x=0.04327*0.001; %m/px
calibration_y=0.04204*0.001; %m/px
er_calibration_x=0.00016*0.001;
er_calibration_y=0.00018*0.001;
%%%%%%%%%%%%%%%%%%%%%%%%%%%%%%%%%%%%%%%%%%%%%%%%%%%%%%%%%%%%%

disp('Reading image ...')
% Get image for background. For background RF is on, gun is off.

bg1 = imread('Scan_1\RF_on_Gun_off_bg.bmp');
bg2 = imread('Scan_2\RF_on_Gun_off_bg.bmp');
bg3 = imread('Scan_3\RF_on_Gun_off_bg.bmp');
bg4 = imread('Scan_4\RF_on_Gun_off_bg.bmp');
bg5 = imread('Scan_5\RF_on_Gun_off_bg.bmp');
bg6 = imread('Scan_6\RF_on_Gun_off_bg.bmp');
bg7 = imread('Scan_7\RF_on_Gun_off_bg.bmp');
% Averaging background.
bg = (bg1+bg2+bg3+bg4+bg5+bg6+bg7+bg7+bg7)/7;
imd_bg = double(bg(:,:,1));

for ii=1:scan_times
switch ii
    case 1
        addpath(genpath('\Scan_1'));
    case 2
        addpath(genpath('\Scan_2'));
```

```matlab
    case 3

        addpath(genpath('\Scan_3'));

    case 4

        addpath(genpath('\Scan_4'));

    case 5

        addpath(genpath('\Scan_5'));

    case 6

        addpath(genpath('\Scan_6'));

    case 7

        addpath(genpath('\Scan_7'));

end


% Read OTR images.

for scan = 1:scan_current_number;

    thisfilename=ii;

    imNo = ii;

    I(scan) = I_start + (scan-1)*I_increment;

    switch scan

        case 1

% Devide the effetive length by 100 to convert to meter unit.

            im = imread('negative\11.bmp');

            tifname='11';

            L_ef(scan) = 9.95/100;

            Er_L_ef(scan) = 0.17/100;

        case 2

            im = imread('negative\12.bmp'); % reading 1.png

            tifname='12';

            L_ef(scan) = 9.91/100;
```

```matlab
            Er_L_ef(scan) = 0.16/100;
    case 3
        im = imread('negative\13.bmp');
        tifname='13';
        L_ef(scan) = 9.91/100;
        Er_L_ef(scan) = 0.16/100;
    case 4
        im = imread('negative\14.bmp');
        tifname='14';
        L_ef(scan) = 9.85/100;
        Er_L_ef(scan) = 0.14/100;
    case 5
        im = imread('negative\15.bmp');
        tifname='15';
        L_ef(scan) = 9.85/100;
        Er_L_ef(scan) = 0.16/100;
    case 6
        im = imread('negative\16.bmp');
        tifname='16';
        L_ef(scan) = 9.87/100;
        Er_L_ef(scan) = 0.19/100;
    case 7
        im = imread('negative\17.bmp');
        tifname='17';
        L_ef(scan) = 9.82/100;
        Er_L_ef(scan) = 0.19/100;
    case 8
        im = imread('negative\18.bmp');
```

```matlab
            tifname='18';

            L_ef(scan) = 9.86/100;

            Er_L_ef(scan) = 0.17/100;

    end

    sg = im; % reading 1.png
imd_sg = double(sg(:,:,1));
pic = (imd_sg-imd_bg);
%imd = imd_sg;
%imd = imd_bg;


% Noise Cleaning.
% Getting red of the dead pixels.
% If there is sudden increase in the pixel brightness,
% Then use the pixel brightnesss of the earlier pixel.
for i = 3:768
for j = 3:576
    if pic(j,i)>500
        pic(j,i)=pic(j-1,i);
    elseif pic(j,i)-pic(j-2,i)>20
            pic(j,i)=pic(j-1,i);
    end
end
end

% Determine image size in pixels.
dim=size(pic);
%dim=size(imd);
dim_x = dim(1);
```

```
dim_y = dim(2);


xunit='m';
yunit='m';


% Beam transverse profiles.
profx = sum(pic,1); % make x projection
profy = sum(pic,2)';% make y projection


xbins=size(profx);
ybins=size(profy);
x=(1:1:xbins(2));
y=(1:1:ybins(2));


% Set Gaussian fit range.
xl = 1;
xr = 766;
yl = 1;
yr = 576;


% Checking.
%plot(x,profx,'k');
%hold on;
%plot(y,profy,'k');
%hold on;


% Initialize fit parameters.
% a1= base. a2 = A; amplitude. a3 = mean. a4 = D; sigma_0. a5 = N;
```

```
a1 = 100;
a2 = 7700;
a3 = 280;
a4 = 39;
a5 = 1;


% SupGau = a(1)+a(2)*exp(-abs(X-a(3))/(a(4))).^a(5); % super gaussian.
% Putting the parameters together.
a0 = [a1,a2,a3,a4,a5];
% Setting fit criteria and use fminsearch optimization.
opts = optimset('TolX',1e-4,'MaxFunEvals',10000,'MaxIter',10000,'Display','on');
% Pass fit parameters to SupGau_devsum.
[fitpara_x,fval_x,flag_x,err_x] = fminsearch(@SupGau_devsum,a0,opts,x,profx);
[fitpara_y,fval_y,flag_y,err_y] = fminsearch(@SupGau_devsum,a0,opts,y,profy);
% Get the fit parameters of x profile.
base_x = fitpara_x(1);
amplitude_x = fitpara_x(2);
peak_center_x = fitpara_x(3);
sig0_x = fitpara_x(4);
N_x = fitpara_x(5);
sig_x(scan,imNo) = sig0_x*(pi/2).^(2/fitpara_x(5)-1);
% Get the fit parameters of y profile
base_y = fitpara_y(1);
amplitude_y = fitpara_y(2);
peak_center_y = fitpara_y(3);
sig0_y = fitpara_y(4);
N_y = fitpara_y(5);
sig_y(scan,imNo) = sig0_y*(pi/2).^(2/fitpara_y(5)-1);
```

```matlab
% Printing out parameters to check.
string_x = [
    num2str(I(scan),'  %2.2f'),'    ', ...
    num2str(imNo,'%d'),'       ', ...
    num2str(base_x,'%12.2f'),'       ', ...
    num2str(amplitude_x,'%12.f'),'          ', ...
    num2str(peak_center_x,'%12.2f'),'       ', ...
    num2str(N_x,'%12.4f'),'    ', ...
    num2str(sig0_x,'%12.2f'),'       ', ...
    num2str(sig_x(scan,imNo),'%12.2f'),'    ', ...
    ];
%disp(string_x);
string_y = [
    num2str(I(scan),'  %2.2f'),'    ', ...
    num2str(imNo,'%d'),'       ', ...
    num2str(base_y,'%12.2f'),'       ', ...
    num2str(amplitude_y,'%12.f'),'          ', ...
    num2str(peak_center_y,'%12.2f'),'       ', ...
    num2str(N_y,'%12.4f'),'    ', ...
    num2str(sig0_y,'%12.2f'),'       ', ...
    num2str(sig_y(scan,imNo),'%12.2f'),'    ', ...
    ];
%disp(string_y);
%sig


% Plot to check.
%plot(x,profx,'k');
```

```matlab
%hold on;

%plot(y,profy,'k');

%hold on;



% Construct fit curve from the fit parameters.

y_fit_x = fitpara_x(1)+fitpara_x(2)*exp( -0.5*(abs(x-fitpara_x(3))/

(fitpara_x(4))).^fitpara_x(5) );

y_fit_y = fitpara_y(1)+fitpara_y(2)*exp( -0.5*(abs(y-fitpara_y(3))/

(fitpara_y(4))).^fitpara_y(5) );


%plot(x,y_fit_x,'r');


%plot(y,y_fit_y,'r');

drawnow

end

end


for scan=1:scan_current_number


% Find mean and standar deviation.

sig_mean_x(scan) = mean(sig_x(scan,:));

sig_mean_y(scan) = mean(sig_y(scan,:));

sig_x_er(scan)   = std(sig_x(scan,:));

sig_y_er(scan)   = std(sig_y(scan,:));


% Converting from pixels to length (in m unit).

sig_mean_x(scan)=sig_mean_x(scan)*calibration_x; %
```

```
sig_mean_y(scan)=sig_mean_y(scan)*calibration_y; %
sig_x_er(scan)= sqrt((sig_x_er(scan)*calibration_x).^2+(sig_mean_x(scan)*
er_calibration_x).^2);
sig_y_er(scan)= sqrt((sig_y_er(scan)*calibration_y).^2+(sig_mean_y(scan)*
er_calibration_y).^2);


% Squared sigma.
sig_sqr_x(scan) = sig_mean_x(scan)*sig_mean_x(scan);
sig_sqr_x_er(scan) = 2*sig_mean_x(scan)*sig_x_er(scan);
sig_sqr_y(scan) = sig_mean_y(scan)*sig_mean_y(scan);
sig_sqr_y_er(scan) = 2*sig_mean_y(scan)*sig_y_er(scan);



%I(scan) = I_start + (scan-1)*I_increment;
%plot(I,sig_mean,'r');
%Get the quarupole strength and its error from the dipole current.
k1(scan) =0.2998*(3.6*0.0001+1945*0.000001*I(scan))/(0.0254*p);


k1_Er(1) =0.2998*((3.6+1.3)*0.0001+(1945+2)*0.000001*I(scan))/(0.0254*p);
k1_Er(2) =0.2998*((3.6-1.3)*0.0001+(1945+2)*0.000001*I(scan))/(0.0254*p);
k1_Er(3) =0.2998*((3.6+1.3)*0.0001+(1945-2)*0.000001*I(scan))/(0.0254*p);
k1_Er(4) =0.2998*((3.6-1.3)*0.0001+(1945-2)*0.000001*I(scan))/(0.0254*p);
er_k1(1)=abs(k1(scan)-k1_Er(1));
er_k1(2)=abs(k1(scan)-k1_Er(2));
er_k1(3)=abs(k1(scan)-k1_Er(3));
er_k1(4)=abs(k1(scan)-k1_Er(4));


k1_er(scan)=max(er_k1);
```

```matlab
k1L(scan) = L_ef(scan)*k1(scan); %k1*L
er_k1L(scan) = sqrt((L_ef(scan)*k1_er(scan) )^2+(Er_L_ef(scan)*k1(scan))^2);
%er_k1L(scan) = L_ef*k1_er(scan);


% Put the parameters together to pass to parabolic fits
FitDatX = [k1L',er_k1L',sig_sqr_x',sig_sqr_x_er'];
FitDatY = [k1L',er_k1L',sig_sqr_y',sig_sqr_y_er'];


end


 X_fit_data = fopen('X_fit_data.txt','w');
 Y_fit_data = fopen('Y_fit_data.txt','w');
 %fprintf(X_fit_data,'%4f %4f %4f %4f \n',k1L(16:31)',er_k1L(16:31)',
 sig_sqr_x(16:31)*10^6',sig_sqr_x_er(16:31)*10^6');
 %fprintf(Y_fit_data,'%4f %4f %4f %4f \n',k1L(2:15)',er_k1L(2:15)',
 sig_sqr_y(2:15)*10^6', sig_sqr_y_er(2:15)*10^6');
 fprintf(X_fit_data,'%4f %4f %4f \n',k1L(16:31)', sig_sqr_x(16:31)'*10^6,
 sig_sqr_x_er(16:31)'*10^6);
 fprintf(Y_fit_data,'%4f %4f %4f \n',k1L(2:15)', sig_sqr_y(2:15)'*10^6,
 sig_sqr_y_er(2:15)'*10^6);
 fclose(X_fit_data);
 fclose(Y_fit_data);

% Converting to cgs (mm and mrad) units.
 [k1L(16:31)' sig_sqr_x(16:31)'*10^6 sig_sqr_x_er(16:31)'*10^6]
 [k1L(2:15)' sig_sqr_y(2:15)'*10^6 sig_sqr_y_er(2:15)'*10^6]
```

```
%Emit_Parabola_Fit_kl_XProjection(k1L,er_k1L,sig_sqr_x,sig_sqr_x_er,me,En,
S12,erS12,scan_current_number);
%Emit_Parabola_Fit_kl_YProjection(k1L,er_k1L,sig_sqr_y,sig_sqr_y_er,me,En,
S12,erS12,scan_current_number);
Emit_Parabola_Fit_kl_XProjection(k1L(16:31),er_k1L(16:31),
sig_sqr_x(16:31)*10^6,sig_sqr_x_er(16:31)*10^6,me,En,En_er,S12,erS12,16);
Emit_Parabola_Fit_kl_YProjection(k1L(2:15) ,er_k1L(2:15),
sig_sqr_y(2:15)*10^6, sig_sqr_y_er(2:15)*10^6, me,En,En_er,S12,erS12,14);
```

B.2   Super Gaussian Fit

"SupGau_devsum.m" function is being called during by "Emit_Calc.m" to fit super Gaussian to beam transverse profile.

```
function chisq = SupGau_devsum(a,X,Y)
% a(1) = base
% a(2) = A;  %amplitude
% a(3) = x0; %center
% a(4) = D;  %sigma_0
% a(5) = N;  %N=2 is nomal Guassian.
          %N<super Gaussian (sharp top).
          %N>Flat top shape Gaussian.
SupGau = a(1)+a(2)*exp( -0.5*(abs(X-a(3))/(a(4))).^a(5) ); % super Gaussian
csq = (Y - SupGau).^2;
chisq = sum(csq);
return
```

B.3 Parabolic Fit

"Emit_Parabola_Fit_kl_XProjection" fits parabola for given rms values, plots the fit and extract the emittance and Twiss parameters from the fit.

```
function varargout = Emit_Parabola_Fit_kl_XProjection(x,erx,y,ery,me,En,
En_er,S12,erS12,NumPoints)


%x
%y
%ery


order = 2; % second order fit
ParNum = order + 1;


% finding row matrix beta
for k=1:ParNum
for i=1:NumPoints
    f(k)=power(x(i),k-1);
    %fprintf('   i=%d  f(%d)=%g \t',i,k,f(k));
    beta_element(k,i)=y(i)*f(k)/(ery(i)*ery(i));
    %fprintf('y(i=%d)=%g ery(i=%d)=%g \n',i,y(i),i,ery(i));
    %fprintf('beta(k=%d,i=%d)=%g \n',k,i,beta_element(k,i));
    beta(k)=sum(beta_element(k,:));
    %fprintf('beta_element(%d,%d)=%g
    %beta(%d)=%g\n',k,i,beta_element(k,i),k,beta(k));
end
end
%beta
```

```
% finding matrix alpha
for k=1:ParNum
for l=1:ParNum
    for i=1:NumPoints
        f(k)=power(x(i),k-1);
        f(l)=power(x(i),l-1);
        alpha_element(k,l,i)=f(k)*f(l)/(ery(i)*ery(i));
        alpha(k,l)=sum(alpha_element(k,l,:));
        %fprintf('alpha_element(%d,%d,%d)=%g alpha(%d,%d)=%g\n',k,l,i,
        alpha_element(k,l,i),k,l,alpha(k,l));
    end
end
end
%alpha


%To find fit parameters, need to invert matrix alpha.
alpha_invert = inv(alpha);
%alpha_invert


% The fit is y = a(1) + a(2)*x + a(3)*x*x
%fit parameters by matrix inversion method
parameter = beta*alpha_invert; %a(l)=parameter(l)
%parameters
fit_m_inver = parameter(1) + parameter(2)*x + parameter(3)*x.*x;
% error on the parameters
er_a = sqrt(diag(alpha_invert));
```

```matlab
%fit parameters by MatLab
par = polyfit(x,y,2);
%par
fit_MatLab = par(3) + par(2)*x + par(1)*x.*x;


%Get Emittance and Twiss parameters from fit
gamma = En/me;
er_gamma = En_er/me;
beta = sqrt(1-1/gamma^2);
er_beta = er_gamma/(gamma^3*beta);


A=parameter(3);
B=-parameter(2)/(2*A);
C=parameter(1)-A*B^2;
erA = er_a(3);
erB = sqrt( (-er_a(2)/(2*A))^2 + (parameter(2)*erA/(2*A^2))^2 );
erC = sqrt((er_a(1))^2 + (-B^2*erA)^2 + (-2*A*B*erB)^2);
%fprintf('A=%g+-%g  B=%g+-%g  C=%g+-%g\n',A,erA,B,erB,C,erC);


emit = sqrt(A*C)/((S12)^2);
er_emit = sqrt( (1/2*A^(-1/2)*A^(1/2)*erA/(S12)^2)^2 +
(1/2*A^(1/2)*A^(-1/2)*erC/(S12)^2)^2 + ( 2*sqrt(A*C)*erS12/(S12)^3)^2 );
emit_n = emit*gamma;
er_emit_n = sqrt((emit*er_gamma*beta)^2+(emit*gamma*er_beta)^2+
(er_emit*gamma*beta)^2);
beta_func = sqrt(A/C);
er_beta_func = sqrt( (1/2*sqrt(1/(A*C))*erA)^2 + (-1/2*sqrt(A/C^3)*erC)^2 );
alpha_func = beta_func*(B + 1/S12);%alpha_func = sqrt(A/C)*(B + 1/S12)
```

```matlab
er_alpha_func = sqrt(((B+1/S12)*er_beta_func)^2 + (beta_func*erB)^2 +
(-beta_func*erS12/(S12)^2)^2 );


figure(1)

set(axes,'FontSize',40)
pardat = errorbar(x,y,ery,'MarkerSize',30,'Marker','.','LineStyle','none',...
'LineWidth',3,...
'DisplayName','Data Points',...
'Color',[0 0 1]);
hold on

%Plot fit done by matrix inversion method.
parfit_m_inver = plot(x,fit_m_inver,'r');
set(parfit_m_inver,'LineWidth',3);


legend('Data','Fit');
set(legend,'Position',[0.73 0.75 0.1 0.1]);
set(legend,'FontSize',40);
set(legend,'FontName','Times New Roman');

hx = xlabel('k_{1}L (m^{-1})','FontSize',48,'FontName','Times New Roman');
hy = ylabel('\sigma^2_x (mm^2)','FontSize',48,'FontName','Times New Roman');
box off; % remove the top and right axes

%set(gca,'ticklength',4*get(gca,'ticklength'));
set(gca,'ticklength',[0.06 0.9]);
fit=title('');
```

```
%fit=title('15.6 MeV, X-Projection: k_{1}L vs \sigma^2');
set(fit,'FontSize',24,'FontWeight','bold','FontName','Times New Roman');
axis([-0.05 0.55 2.3 3.2]); %axis([xmin xmax ymin ymax])
%axis('FontSize',28);


saveas(fit,'Emit_Calc_plots\par_fit_x.fig','fig');
saveas(fit,'Emit_Calc_plots\par_fit_x.eps','epsc');
saveas(fit,'C:\Users\sadiq\Desktop\IPAC12\Paper\par_fit_x.eps','epsc');
saveas(fit,'Emit_Calc_plots\par_fit_x.png','png');
drawnow


fprintf('x-projection:\n\nemit=%.3f +- %.3f mm*mrad, emit_norm=%.2f +-
%.2f mm*mrad \n\n', emit, er_emit, emit_n, er_emit_n);
fprintf('beta=%.2f +- %.2f m, alpha=%.2f +- %.2f rad \n\n', beta_func,
er_beta_func, alpha_func, er_alpha_func);
fprintf('parabola fit for y-projection (y in mm unit): \n y = (%.5f +-%.5f)
+ (%.5f+-%.5f)*x + (%.5f+-%.5f)*x.*x \n\n', parameter(1),er_a(1),
parameter(2),er_a(2), parameter(3),er_a(3));
return
```

References

[1] S. Chemerisov. and C. D. Jonah, in *Proc.* JPOS09, Newport News, Virginia.

[2] North Carolina State University, *http://www.ne.ncsu.edu/nrp/ips.html*, Intense Positron Beam, Nuclear Reactor Program, 2013-06-28.

[3] M. N. Rosenbluth, *Phys. Rev.*, 18, 1014 (1950).

[4] R. C.Walker *et al.*, *Phys. Rev. D*, 49, 5671 (1994).

[5] J. Arrington, *Phys. Rev. C*, 68, 034325 (2003).

[6] R. C. Walker, *Ph.D. Thesis*, California Institute of Technology (1989).

[7] H.W. Koch & J.W Motz, *Rev. Mod. Phys.*, 31, 920 (1959).

[8] K. S. Krane, *Introductory Nuclear Physics.* (John Wiley & Sons, NY, 1988).

[9] NIST, *http://physics.nist.gov/cgi-bin/Xcom/xcom2*, NIST XCOM, 2013-05-03.

[10] M. Conte, & W. W. Mackay, *An Introduction To The Physics Of Particle Accelerators*, World Scientific, New York, 2008.

[11] V.L Ginzburg & I.M. Frank, *Sov. Phys. JETP*, 16, 15 (1964).

[12] K.T. McDonald and D.P. Russell, Fron. of Par. Beams Obser. Diag. and Cor. 08544, (1988).

[13] Y. Kim *et al.*, in *Proc. FEL*2008, Gyeongju, Korea.

[14] D.F.G. Benedetti, *et al.*, Tech. Rep., DAFNE Tech. Not., Frascati, Italy (2005).

[15] S.Y. Lee, *Accelerator Physics*, 2nd ed. (Singapore: World Scientific, NY, 2004).

[16] B. Gitter, Tech. Rep., Los Angeles, USA (1992).

[17] Muons, Inc., *http://public.muonsinc.com/*, 2013-08-08.

[18] CERN, *http://geant4.cern.ch/*, 2013-08-08.

[19] SAINT-GOBIAN, *http://www.detectors.saint-gobain.com*, SAINT-GOBIAN CRYS-
     TALS Technical Information Notes, 2013-06-11.

[20] F.J. Decker, NASA STI/Recon Tech. Rep. N 1994.